Title

Crosswell traveltime tomography in three dimensionsCrosswell Traveltime Tomography in 3-D

Journal

Geophysics, 67(3)

ISSN

0016-8033

Authors

Washbourne, John K
Rector, James W
Bube, Kenneth P

Publication Date

2002-05-01

DOI

10.1190/1.1484529

Peer reviewed

Crosswell traveltime tomography in three dimensions

John K. Washbourne*, James W. Rector‡, and Kenneth P. Bube**

space**ABSTRACT**

Conventional crosswell direct-arrival traveltime to- mography solves for velocity in a 2-D slice of the subsur- face joining two wells. Many 3-D aspects of real crosswell surveys, including well deviations and out-of-well-plane structure, are ignored in 2-D models. We present a 3-D approach to crosswell tomography that is capable of handling severe well deviations and multiple-profile datasets.

Three-dimensional pixelized models would be even more seriously underdetermined than the pixelized models that have been used in 2-D tomography. We, therefore, employ a thinly layered, vertically discontinu- ous 3-D velocity model that greatly reduces the number of model parameters. The layers are separated by 2-D in- terfaces represented as 2-D Chebyshev polynomials that are determined using a priori structural information and remain fixed in the traveltime inversion. The velocity in each layer is also represented as a 2-D Chebyshev polynomial. Unlike pixelized models that provide lim- ited vertical resolution and may be overparameterized horizontally, this 3-D model provides vertical resolution comparable to the scale of wireline logs, and reduces the degrees of freedom in the horizontal parameterization to the expected in-line and out-of-well-plane horizontal resolution available in crosswell traveltime data.

Ray tracing for the nonlinear traveltime inversion is performed in three dimensions. The 3-D tomography

spaceproblem is regularized using penalty constraints with a continuation strategy that allows us to extrapolate the velocity field to a 3-D region containing the 2-D cross- well profile. Although this velocity field cannot be ex- pected to be accurate throughout the 3-D region, it is at least as accurate as 2-D tomograms near the well plane of each 2-D crosswell profile. Futhermore, multiple-profile crosswell data can be inverted simultaneously to re- solve better the 3-D distribution of velocity near the profiles.

Our velocity parameterization is quite different from pixelized models, so resolution properties will be differ- ent. Using wave-modeled synthetic data, we find that near horizontal raypaths have the largest mismatch be- tween ray-traced traveltimes and traveltimes estimated from the data. In conventional tomography, horizontal raypaths are essential for high vertical resolution. With our model, however, the highest resolution and most accurate inversions are achieved by excluding raypaths that travel nearly parallel to the geologic layering. We perform this exclusion in both a static and model-based manner. We apply our 3-D method to a multiple-profile crosswell survey at the Cymric oil field in California, an area of very steep structural dips and significant well tra- jectory deviations. Results of this multiple-profile 3-D tomography correlate very well with the independently- processed single profile results, with the advantage of an improved tie at the common well.

space

spaceINTRODUCTION

Crosswell direct arrival traveltime tomography for a single profile between two wells is inherently a 2-D problem. Al- though the subsurface of the Earth is three dimensional, the energy recorded in a crosswell dataset that influences direct arrival traveltimes has traveled mostly through a quasi–2-D region close to a 2-D surface joining the wells. Because the

spacevelocity in this quasi–2-D region is all that we can hope to determine from the traveltime data, approaches to crosswell tomography have generally attempted to determine a velocity profile defined on a planar 2-D slice. Many 3-D aspects of the geometry either have to be ignored in a planar 2-D model or included with great effort. Most wells are not perfectly straight and vertical. Each well separately may not even stay within a single plane, and it is not uncommon for two wells together to space

Manuscript received by the Editor September 17, 1999; revised manuscript received October 24, 2001.
*TomoSeis, Inc., 6316 Windfern, Houston, Texas 77040. E-mail: jwashbourne@corelab.com.
‡University of California, Berkeley, Department of Civil Engineering, 412 Davis Hall, Berkeley, California 94720. E-mail: jwrector@lbl.gov.
**University of Washington, Department of Mathematics, Box 354350, Seattle, Washington 98195. E-mail: bube@math.washington.edu.

spacebe far from coplanar. In these situations, the quasi–2-D region of the subsurface influencing the crosswell traveltimes is not close to any 2-D plane. Even if the two wells are coplanar, energy can travel along paths out of that plane if there is out- of-plane dip in the structure or out-of-plane velocity variation near the wells.

Multiple-profile crosswell tomography can be handled as a suite of separate single-profile 2-D problems, each providing the velocity field on a 2-D slice of the subsurface. Incorporating several separate 2-D profiles into one consistent 3-D model is not easy, however, particularly when there are misties between profiles at wells involved in more than one profile. The 2-D profiles can be extended beyond the well planes using inter- polation, extrapolation, or least-squares fitting to construct a 3-D model that is approximately consistent with all of the 2-D profiles. In most multiple-profile situations, these 2-D profiles are not dense enough to get an accurate 3-D model.

Crosswell tomography in realistic geometries thus faces a serious difficulty. Because of the 3-D aspects of the problem mentioned above, we need to have a 3-D velocity field to trace rays accurately, but the traveltime data determine only one (or several) 2-D slices of the velocity field.

We present here a strategy for overcoming this difficulty. Instead of a two-stage process of determining 2-D slices and then extrapolating them to obtain a 3-D model, we will deter- mine the 2-D profiles and their extrapolation to 3-D together simultaneously, obtaining directly a 3-D velocity model. Much of this 3-D velocity model will be inaccurate because there are insufficient data to determine it accurately. But the parts in the quasi–2-D regions between the wells will be recovered as accu- rately as they would be using a 2-D approach. Two-dimensional tomograms can be extracted from this 3-D model: the rays tell us where the 2-D surfaces are, and these surfaces can be pro- jected onto nearby planes for display purposes.

Our strategy is able to handle well deviations and out-of- plane dip, and works effectively for both single-profile and multiple-profile tomography problems. The four aspects of our strategy that we discuss in detail in this paper are the following. First, we parameterize our velocity model in a manner appro- priate for this combined tomography and extrapolation, using a priori structural information to help determine

the extrap- olation. Second, the ray tracing is performed in three dimen- sions in the tomography algorithm. Third, we regularize the severely underdetermined 3-D tomography problem in a way that solves the quasi–2-D problems accurately. Fourth, we edit the traveltime data to remove errors due to the inconsistencies between ray-traced traveltimes and picked traveltimes when large velocity contrasts generate rays that follow head waves. Each of these four aspects plays an important role in the overall success of our strategy.

Conventional crosswell direct-arrival traveltime tomogra- phy is quite sensitive to the choices of model parameteri- zation and/or the regularization (smoothing) of the inver- sion, and provides limited resolution (Michelena and Harris, 1991; Pilkington and Todoeschuck, 1991; Williamson and Worthington, 1993; Michelena 1993; Rector and Washbourne, 1994). When using pixelated or gridded models, the system of equations describing the tomographic problem can often be un- derdetermined (Dines and Lytle, 1979). The traveltime data are usually insufficient in number and angular coverage to resolve fine-scale lateral variations; thus, a pixelized formulation with a spaceregular grid often introduces more degrees of freedom than the data can support (Michelena and Harris, 1991). The unresolved parts of the problem, primarily high-frequency horizontal vari- ations in the model, are unstable and can become amplified by noise in the data (Squires and Cambois, 1992). Consequently, substantial work has been done in devising appropriate model parameterization and regularization schemes (Michelena and Harris, 1991; Squires et al., 1994; Bube and Langan, 1994, 1997, 1999; Carrion et al., 1995; Nemeth et al., 1997; Lazaratos and Marion, 1997). Phillips and Fehler (1991) give an overview of popular methods, including constraining model parameter up- dates and smoothing least-squares solutions.

In this study, we describe a new 3-D model parameterization. We depart from the conventional pixelated model and adopt the approach of Lazaratos and Marion (1997). They employ a thinly layered, vertically discontinuous 2-D velocity model, sparsely noded in thehorizontal direction. Limiting thenumber of parameters in the horizontal direction makes the traveltime inversion problem better conditioned by removing degrees of freedom that the traveltime data cannot resolve. The fine vertical source and receiver spacing of modern crosswell surveys, however, can provide high vertical resolution. The parameterization of Lazaratos and Marion achieves vertical resolu- tion comparable to wireline logs, much higher than is evident in most pixelated inversions. Thus, a layered parameteriza- tion is clearly more effective for sedimentary sections than the pixelated approach.

While Lazaratos and Marion's (1997) model parameteri- zation was effective in two dimensions, the ability to handle crosswell geometries in the presence of steep structural dips or well deviations requires 3-D traveltime modeling capability. We extend their approach to 3-D models, modifying it appro- priately for use with either single-profile or multiple-profile crosswell surveys. Like Lazaratos and Marion, we use a thinly layered, vertically discontinuous velocity model; our layers are separated by 2-D interfaces represented as third-order 2-D Chebyshev polynomials. Instead of nodes in the horizontal di- rections, we again use third-order 2-D Chebyshev polynomials to represent the horizontal variation of velocity within each layer. The small number of parameters devoted to horizontal resolution is consistent with both the low horizontal resolution expected in the plane of the wells and the even lower hori- zontal resolution expected as we move away from the quasi– 2-D regions that influence the crosswell traveltimes. Although third-order Chebyshev polynomials cannot fully capture the horizontal variation of velocities across an abrupt discontinu- ity such as a fault, they represent a reasonable approximation to the potential horizontal resolution available in direct arrival traveltime tomography (Williamson and Worthington, 1993; Rector and Washbourne, 1994).

There are many examples of using surfaces for ray trac- ing and traveltime inversion. Chiu et al. (1986) and Chiu and Stewart (1987) employ polynomials to represent surfaces of arbitrary geometry for the inversion of surface reflection and vertical seismic profile data, but model velocity as homoge- nous between layers. Guiziou et al. (1996) use triangular mesh surfaces to represent arbitrary structure for the inversion of surface reflection data.

Grechka and McMechan (1996) use Chebyshev polynomi- als to represent both the velocity model and raypaths through it. One particular advantage of this parameterization is that spacetraveltime and derivatives of traveltime can be calculated explicitly, and thus raypaths can be found efficiently using, for example, conjugate gradients or the Newton method. The Grechka and McMechan parameterization was designed to represent smoothly varying heterogeneities, however, and may lose applicability in the presence of discontinuities or hetero- geneities at crosswell scales.

The problem of estimating 3-D velocity structure from mul- tiple crosswell profiles has only recently been addressed. In general, published work in this area involves independently processing a set of 2-D profiles, and then performing some type of geostatistical interpolation or extrapolation to fit 3-D pop- ulation distributions of parameters (e.g., slowness). Hyndman and Harris (1996) propose resolving "multi–2-D" structure by co-inverting multiple profiles with a statistical scheme that limits the variations in slowness populations. Eppstein and Dougherty (1998a) present a method for 3-D modeling requir- ing decomposition into independent 2-D slices; the final 3-D distribution is recovered by statistical operations on the in- dependently processed slices. The geometry for the synthetic example they present consists of twelve vertical boreholes that effectively surround the 3-D model. Eppstein and Dougherty spacesubsurface. The model consists of two parts: a structural part made of vertically discontinuous layers that mimic geologic contours, and a functional part that for traveltime tomography is used to represent slowness (reciprocal velocity). Both the structural part (surfaces) and the functional part (subsurface parameters) are specified by Chebyshev polynomials.

Figure 1 is a schematic showing a vertical slice through our model parameterization. Each of the surfaces $Z_i(x, y)$ is represented by a third-order 2-D Chebyshev polynomial. The slow- ness within each layer (bounded by a surface above and below) is specified with a similar third-order 2-D Chebyshev polyno- mial, $S_i(x, y)$. This type of stratification is "earth-like," with high vertical resolution (Lazaratos and Marion, 1997). Further, the polynomials can represent velocity varying laterally in two dimensions with relatively few parameters. The combination allows the specification of velocity, and other quantities of interest, anywhere within a particular 3-D volume. Hence, we are able to obtain estimates of 3-D velocity fields from multiple profile crosswell data.

The 2-D Chebyshev polynomials are a limited tensor product of 1-D Chebyshev polynomials, keeping only terms of up to third order. Equation (1) shows the form of the polynomials:

space(1998b) present a variant of their approach when there are fewer boreholes.

In the next two sections, we describe our 3-D model formu-

$$\text{space}F(x, y) = + C$$

$$\text{space}_0 + C_1x + C_2y + C_3xy + C_4(2x - 1)$$

space+ $C_5(2y$
space− 1) + $C_6(2x$
space− 1)y + $C_7(2y$
space− 1)x

space3-D ray bending. We then describe a continuation strategy to smoothing constraints for our 3-D model parameterization— an approach to regularization that greatly improves resolution. Using wave-modeled synthetic traveltimes, we find thatthe reg- ularization parameters with this approach can be decreased an order of magnitude relative to standard weighted least-squares regularization. This removes, as much as possible, the effects of the type and level of regularization from the tomographic results. Also using wave-modeled synthetic traveltimes, we demonstrate how the limitation of certain offset ranges in the data corresponding generally to head waves—raypaths travel- ing nearly parallel to geologic layering—improves the robust- ness and resolution of crosswell tomographic inversion when applied with our model parameterization. In the final sections of the paper, we demonstrate the continuation strategy with an acoustic finite-difference synthetic example, and use real data to illustrate the simultaneous resolution of a single 3-D model from a multiple-profile crosswell survey at the Cymric oil field in California, an area of steep structural dips and significant well trajectory deviations.

The effects of anisotropy in real crosswell seismic data should be included in the modeling and inversion of traveltimes (Saito, 1991; Chapman and Pratt, 1992; Pratt and Chapman, 1992; Michelena, 1993; Michelena et al., 1993; Williamson, 1993a,b; Grechka and McMechan, 1996, Bube and Meadows, 1998). Our formulation can be modified to include anisotropy in the mod- els (Washbourne et al., 1999). In this paper, we restrict our attention to the isotropic case.

MODEL FORMULATION

We focus on modeling for traveltime tomography of cross- well data. The model framework introduced here has also been used for crosswell reflection imaging (Jervis et al., 2000), and can be extended for other quantities of interest in the

space+ $C_8(4x - 3x) + C_9(4y - 3y)$. (1)

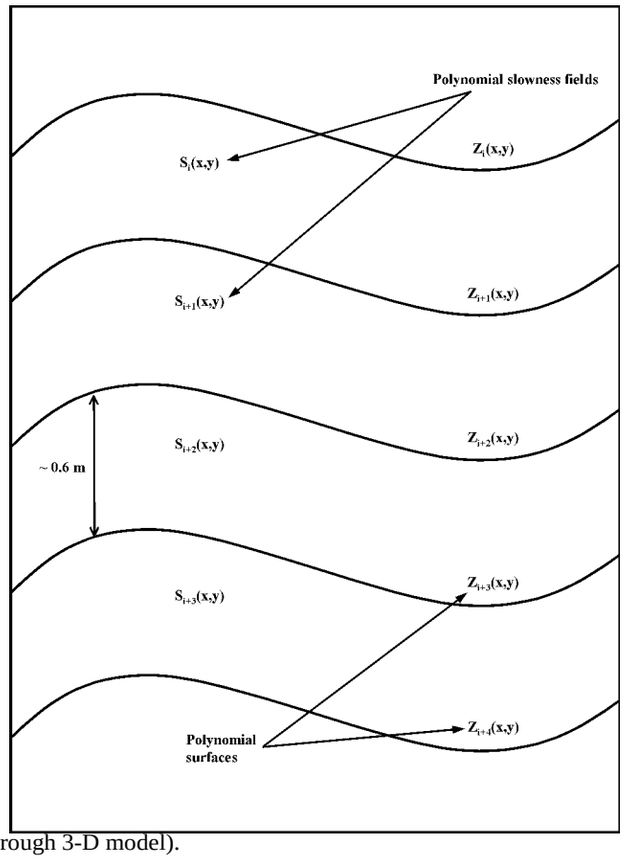

FIG. 1. Schematic of common earth model geometry (vertical slice through 3-D model).

spaceThe coefficients C_0 through C_9 weight the contributions of the orders of the polynomial. We have a constant term (C_0), two first-order terms (C_1 and C_2), three second-order terms (C_3 through C_5), and four third-order terms (C_6 through C_9). By weighting the coefficients it is possible to fit surfaces of varying spatial smoothness. These ten coefficients provide essentially cubic variability in structure and velocities. Although certainly insufficient to represent some scales of geologic heterogene- ity, a large class of real world crosswell problems can be adequately treated with this representation.

The structural part of the model is constrained to be geologi- cally realistic by fitting the surfaces to horizon picks from wire- line log correlations in the wells. Constraining the geometry of the surfaces is the key factor in creating high-resolution images. In fact, Michelena et al. (1995) showed that if the surfaces are not constrained, the resolution can be significantly degraded. The coefficients for the Chebyshev polynomials are found by singular value decomposition of the log correlation data. Figure 2 shows a real example of different order surfaces fit to horizon picks from a series of five deviated wells in Chevron's Buena Vista Hills field in Kern County, California (Langan et al., 1998). The horizon picks from wireline logs are shown as the three boxes in each well in Figure 2a. Zero-order surfaces are horizontal, and would be used only in the absence of a pri- ori geologic orwell-log information about structure. First-order

spacesurfaces are constant dip and plunge planes, appropriate when there is limited well-log information available (Figure 2b). Second- and third-order surfaces are appropriate when there exists a priori information from a number of neighboring wells in areas of structural complexity, as in Figures 2c and 2d.

The model used for tomography is obtained by interpolating the initial surfaces to a nominal vertical spacing of less than 1 m. Figure 3 demonstrates an elevation view of a series of surfaces in the vicinity of a pair of deviated wells that for clarity have been interpolated to the coarser nominal spacing of 5 m. After this initial interpolation of the a priori "horizon pick" surfaces, the structural part of the model remains unchanged throughout the traveltime inversion procedure; only the velocities in the layers between the structural surfaces can change. Ultimately crosswell reflections (or other types of data) could be used to refine the structural part of the model.

TRAVELTIME CALCULATION AND RAY TRACING

The type of ray tracing used in crosswell tomography has been studied extensively (Langan et al., 1985; Virieux and Farra, 1991). Many early crosswell tomography stud- ies assumed raypaths were straight (Dines and Lytle, 1979; Scales, 1987; Phillips and Fehler, 1991), but recognized the nonlinearity of raypath with velocity. Iterative solutions to space

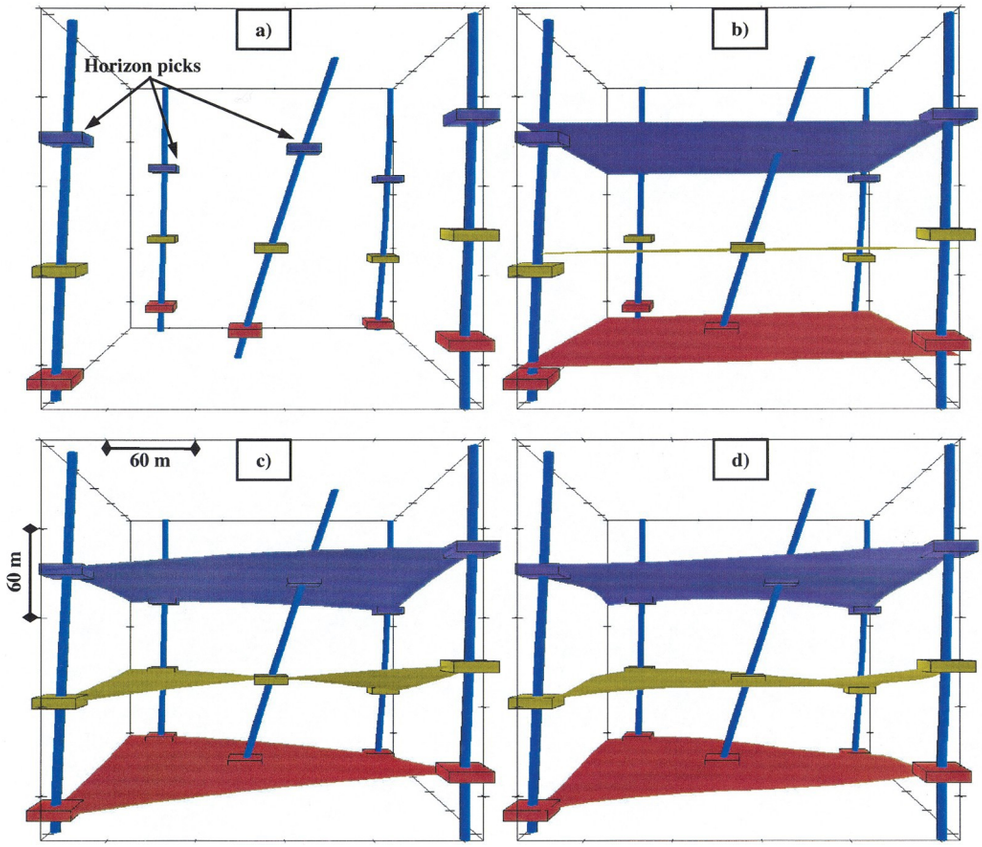

FIG. 2. Chebyshev polynomial surfaces fit to horizon picks in deviated wells: (a) horizon picks, (b) first-order surfaces fit to horizon picks, (c) second-order surfaces fit to horizon picks, and (d) third-order surfaces fit to horizon picks.

spacethe tomographic problem require ray tracing for accuracy (Bregman et al., 1989), particularly when strong velocity inho- mogeneities are present. Although the "shooting method"— propagation of rays by successive application of Snell's law at interfaces or cell boundaries—has widespread use, high wavenumber fluctuations in velocity can cause it to fail (Luo and Schuster, 1991). This has the effect of destabilizing iter- ative solutions for the tomography problem that rely on ray tracing (Phillips and Fehler, 1991).

Another alternative is to use the finite difference solution of the eikonal equation (Vidale, 1988), with raypaths calculated to be locally normal to wavefronts (Ettrich and Gajewski, 1998). This technique uses specification of velocity on a grid, and requires many more nodes horizontally than can be resolved by the inversion of crosswell direct arrival traveltimes. In addi- tion, the computational overhead to obtain accurate raypaths through high vertical resolution models is large even in two dimensions, and for three dimensions becomes prohibitively expensive for iterative ray tracing.

The "bending method," in contrast, is a two-point pertur- bative approach that relies on Fermat's principle of least time (Julian and Gubbins, 1977). The two-point method can provide solutions where a propagator method can fail. Chiu et al. (1986) point out another clear advantage of the bending method: it can be expected to operate faster than the shooting method for 3-D problems. Grechka and McMechan (1996) employ the

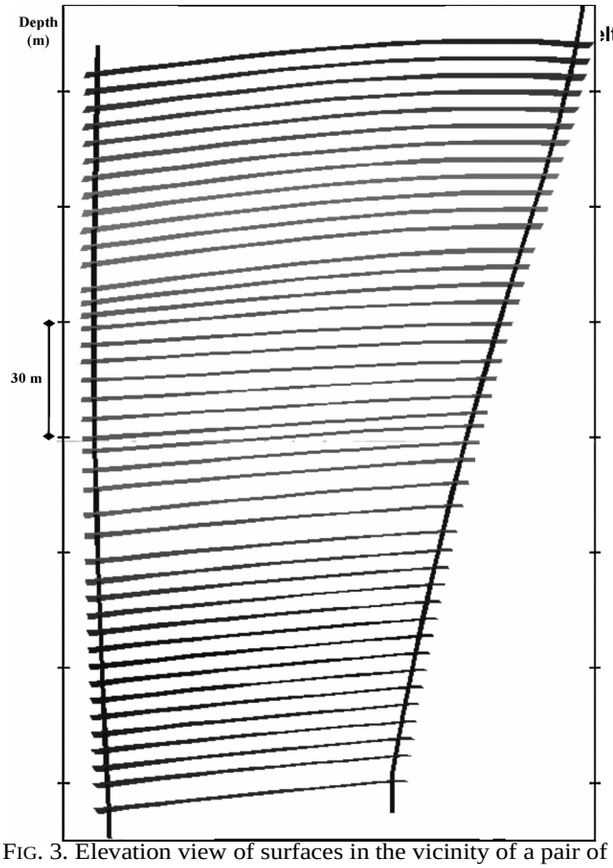

FIG. 3. Elevation view of surfaces in the vicinity of a pair of deviated wells interpolated to nominal spacing of 5 m.

spacebending method with a Chebyshev polynomial parameteriza- tion for both velocities and raypaths, and they note that the resulting explicit form for traveltime is advantageous. We ob- tain similar algorithmic advantages with our parameterization, including analytic calculation of traveltime and derivatives of traveltime. The individual third-order Chebyshev polynomials are continuously differentiable laterally throughout the model, and the small number of parameters required improves the stability and robustness of both the forward problem (ray tracing) and the inverse problem (velocity inversion).

There are two assumptions involved in the forward modeling and traveltime calculation: (1) slowness within a layer is a func- tion of x and y, but invariant of z; and (2) raypaths are straight lines between layer boundaries. These assumptions hold to first order because layer spacing is chosen small compared to wave- length for most crosswell data. The traveltime integral for a single layer is given by equation (2), and is calculated in para- metric form in Appendix A. The corresponding geometry is shown in Figure 4.

$$t = \int_A^B S(x, y)\, dl, \qquad (2)$$

where t is the traveltime, $S(x, y)$ is the polynomial slowness within the layer, A and B are the intersection locations of the raypath with the surfaces that bound the layer, and dl is a differential element of length along the path from A to B. The total traveltime for a ray intersecting many layers is given by the sum over the individual segments.

To trace rays with the bending method, we start with the straight ray connecting source and receiver, and minimize traveltime by iteratively finding perturbations to the raypath. Due to the vertical stratification of the model, z on the surfaces is a function of x and y, and the dimensionality of the problem is reduced to solving only for the updates to x and y at the intersections of the raypath with the surfaces.

Using Newton's method to solve the nonlinear ray-tracing problem yields an elegant structure for the successive lin- earized problems. According to Fermat's principle, we want the raypath with the minimum traveltime. Thus to compute first arrivals, the objective function that we minimize is traveltime, and derivatives of this functional with respect to the intersection lo- cations can be determined in closed form. These partials only involve terms from adjacent layers, and the Hessian matrix of

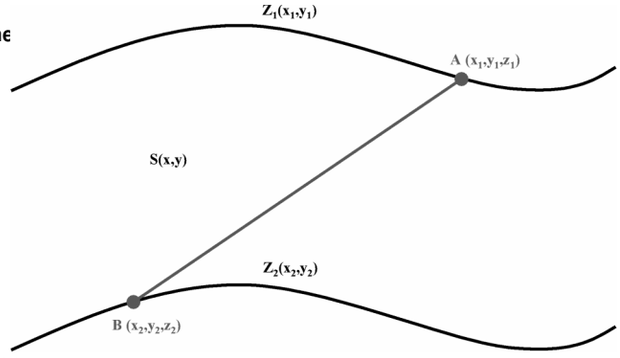

FIG. 4. Schematic of geometry for traveltime calculation within a layer.

spacesecond derivatives is therefore band-diagonal and symmetric with nonzero elements in only three super-diagonals. The lin- ear systems are quickly solved using matrix decomposition or factorization. The derivatives and linear system used for ray tracing are shown in more detail in Appendix A.

VELOCITY INVERSION AND THE CONTINUATION STRATEGY

A simple definition of tomography is the reconstruction of a field from line integrals through the field (Dines and Lytle, 1979; Woodward, 1992). As many researchers have noted (e.g. Scales, 1987; Bregman et al., 1989; Phillips and Fehler, 1991), the line integrals for traveltime tomography (raypaths) are nonlinear with respect to the field we seek to reconstruct (ve- locity distribution). Therefore, most tomography algorithms linearize the problem around a background velocity and itera- tively seek updates to the velocity. For a particular source and receiver geometry and velocity parameterization, traveltimes are modeled by computing line integrals through the veloc- ity field. Then a system of equations is solved that relates the sensitivity of traveltime with respect to changes in the veloc- ity parameterization (Fre´chet derivatives) to the predicted er- ror of the modeled traveltimes. In general the $\mathcal{L}_2$ norm (least squares) of the error is minimized, but other norms have also been used (Scales and Gersztenkorn, 1988; Bube and Langan, 1997, 1999).

In our formulation of the linear system for traveltime in- version, we exploit the analytic form of the expression for traveltime [Appendix A, equation (A-7)] in the calculation of the Fre´chet derivatives. In each layer, we have to solve for ten coefficients, which is fewer parameters than we need for a convenient pixelized or gridded model with equivalent lat- eral resolution. For example, a third-order polynomial in one dimension can be represented by 4 grid points, so an evenly spaced Cartesian grid with similar lateral resolution requires 16 grid points for the 2-D horizontal variables. Although the choice to use Chebyshev polynomials results in fewer model parameters and thus a more well-conditioned inverse, using polynomials requires that some type of regularization be ap- plied within the inversion scheme in order to avoid extreme variations in velocity in areas of the model that have poor ray coverage.

The subject of constraints or regularization for crosswell tomography has been extensively covered (see, for example, Meyerholtz et al., 1989; Michelena and Harris, 1991; Peterson and Davey, 1991; Phillips and Fehler, 1991; Squires and Cambois, 1992; Michelena, 1993; Bube and Langan, 1994, 1999; and many others). Michelena (1993) and Squires et al. (1994) point out that for 2-D pixelized inversion, the null-space (con- sisting primarily of the high-wavenumber horizontal compo- nents of slowness) is unstable and can be amplified by noise in the data if left unconstrained.

While some type of constraints are necessary, care must be exercised in choosing the proper implementation, be- cause the regularization will overprint inversion results. Con- volutional quelling (Meyerholtz et al., 1989) is an example of this—where for weighted least squares, off-diagonal terms of the weighting matrix affect the solution similar to a 2-D nearest-neighbor smoothing function. Certainly some of the "regularization overprint," which in general amounts to spacesmoothing, may be preferable to what Phillips and Fehler (1991) describe as high-wavenumber fluctuations in velocities, but we should exercise care in order to achieve the maximum resolution that can be obtained from the traveltime data. This implies using the minimum constraints that are required to stabilize the problem.

Bube and Langan (1994, 1999) describe the effect of em- ploying regularization as changing an ill-posed problem into a "nearby well-posed problem." The difficulty is to implement regularization such that the solution to the "nearby" prob- lem remains very nearly a solution to the original problem. Bube and Langan (1994, 1999) solve separate iterative nonlin- ear problems for fixed regularization, successively decreasing the level of the constraints until the data, not the regulariza- tion, is in control. They call this "smoothing constraints with a continuation strategy," and refer to each of the fixed regular- ization problems as a "continuation step." The key idea they present is to use the final solution from the previous "step" (fixed regularization problem) as the initial model for the it- erative solution to the next, less regularized, problem (Bube and Langan, 1994, 1999). Others have proposed similar ideas, including Williamson (1990), who successively increases the number of pixels, and Nemeth et al. (1997), who use a very similar philosophy and call it "dynamic smoothing."

Bube and Langan (1994, 1999) apply the smoothing con- straints as penalties that force model smoothness. The penal- ties are applied by adding rows to the system of equations used in the inversion, similar to Tikhonov regularization (Tikhonov and Arsenin, 1977). For the common earth model introduced here, vertical or horizontal smoothness is achieved by forcing the appropriate derivative of slowness to be small. The vertical penalty is computed using numerical differences of polynomial coefficients in adjacent layers, and horizontal penalties can be applied directly to the polynomial coefficients in closed form. For the crosswell 3-D problem, we apply two horizontal penal- ties, one for derivatives along the interwell plane (tangential), and one for derivatives perpendicular to the interwell plane (normal). Application of the horizontal penalties prevents ex- treme variations in velocity in areas where there is little ray coverage.

The overall continuation strategy is to reduce the penalties, forcing model smoothness gradually as the inversion process proceeds. In general, the fixed iterative nonlinear problem in each continuation step is considered "solved" when the ob- jective function has reached a minimum for that level of reg- ularization. Usually, it requires more nonlinear iterations to reach a minimum when the regularization is weak. Ultimately, the penalties can be made very small, and the data itself will control the inversion results. Further, we understand the physi- cal correlation of regularization for the continuation approach. Where

there is no data controlling the values of model parame- ters (the “null space” of the traveltime problem), the penalties force the model to be smooth.

SYNTHETIC MODELS

To investigate the resolution and sensitivity of our crosswell tomography approach, we inverted traveltimes picked from a synthetic dataset created using a fourth-order in space, second- order in time 2-D acoustic wave-equation finite-difference algorithm (Kelly et al., 1976). To give our inversion method a

spacenontrivial test, we chose to use wave equation modeling to generate synthetic data with a typical crosswell frequency spec- trum (center frequency 700 Hz).

To characterize both the vertical and horizontal resolution of the method, we created two models, both with fine vertical structure, but one simulating the presence of a vertical fault. Both models are shown in Figure 5, and we will refer to them hereafteras the“1-D model” (Figure 5b), and the“fault model” (Figure 5c). The velocity models were created from a blocked well log from the McElroy oil field in West Texas (Harris et al., 1995). Figure 5a shows the sonic velocities from one of the wells in McElroy field. Both the 1-D and fault models were created from the log with a minimum layer thickness of

0.6 m, and both show the 30-m thick low-velocity reservoir zone at approximately 870 m depth. The models also demonstrate rapid vertical velocity variations. Velocities range from 3650 to 7000 m/s, as at McElroy field. The fault model is very similar to the 1-D model except for the 30-m depth interval from 840 to 870 m. Over this range, the model simulates a vertical fault 60 m from the left well with a vertical throw of 6 m.

The crosswell geometry used to create the synthetic data was identical for both models, and consisted of evenly spaced sources and receivers over a depth range of 730 to 915 m. Source/receiver spacing was 1.5 m, with 121 positions simulated in each well for a total of 14641 traces. We estimated traveltimes from the finite-difference modeled data in a manner consistent

spacewith the approach used on real data collected with comparable frequencies and geologic conditions. Although our modeling did not incorporate all the effects observed in real crosswell data sets (e.g., source and receiver radiation patterns, shear waves, conversions, tubewaves, etc.), it does contain some more critical aspects of real wave behavior such as the Fresnel zone and wide-angle (head wave) effects. Because of some of these effects, it was impossible to estimate traveltimes for certain parts of the dataset, primarily those corresponding to the up- per part of the model. Figure 6 shows the traveltimes picked from the finite-difference data for the 1-D model in source- receiver coordinates. We could not determine traveltimes for the white area that corresponds to shallow source and receiver depths because of waveform complexity.

THE EFFECTS OF APERTURE LIMITATION

For real crosswell data, the waveforms in the vicinity of the first arrivals for small vertical offsets are usually very complex (for this paper, “offset” is defined as source depth minus receiver depth). For horizontal layering, the direct arrivals at small offsets have raypaths that travel nearly parallel to the lay- ering and, for moderate velocity contrasts, the first arrivals are generally head waves. It is common practice for many of these nearly horizontal rays to be excluded from crosswell tomography because the traveltimes cannot be determined (Michelena

space

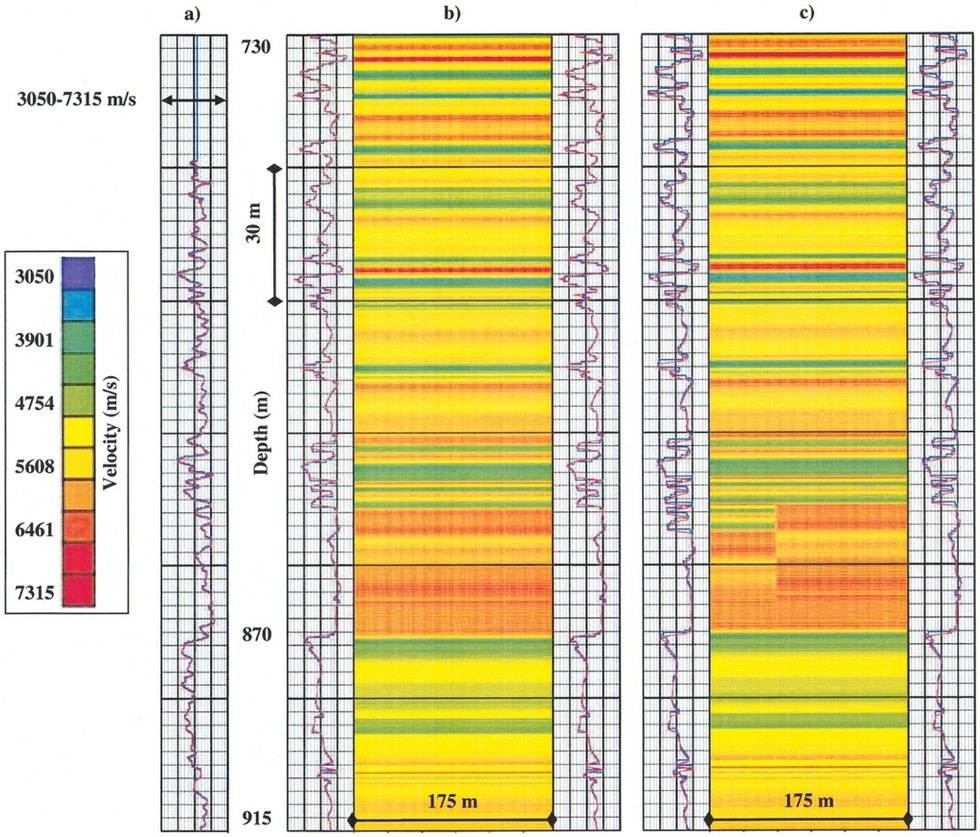

FIG. 5. Synthetic McElroy models: (a) sonic log velocities from a well in McElroy field, (b) 1-D model, and (c) fault model.

spaceet al., 1995). Our approach, however, is to discard intentionally certain angle/offset ranges in the data that correspond to these nearly horizontal rays in order to improve the efficiency of our tomography algorithm.

Figure 7 shows two common offset gathers from the 1-D model (Figure 5b) acoustic finite-difference data, one small offset (offset 45 m, angle from the horizontal 14°), and one large offset (offset 90 m, angle 28°). Red and blue lines in Figure 6 show the locations of the gathers in source-receiver coordinates. I=)m the syn- thetic data and traveltimes ray traced through the true model are shown with in— r (small offset), the difference between the ray-traced times (upper line) and the hand-picked times (lower line) is clear. This figure illustrates the angular or offset dependence of the mismatch between ray-theoretical traveltimes and traveltimes picked from wave-modeled data. For the smaller angles/offsets, there is a large mismatch be- tween ray-traced and wave-modeled times. This is due to the fact that in the presence of even moderate velocity contrasts, arrival times for the near offsets are multivalued, and show evidence of both direct and head wave energy. Inclusion of this multivalued data into ray-theoretical traveltime tomogra- phy introduces the necessity to discriminate between the first- arrival and other arrivals (e.g., the direct arrival). This gener- ates at least three alternatives for the tomographic problem for realistic crosswell seismic waves:

1) Consistently determine traveltimes on the first-arriving energy—what Woodward (1992) refers to as "Fermat path" arrivals. This can be exceptionally difficult because

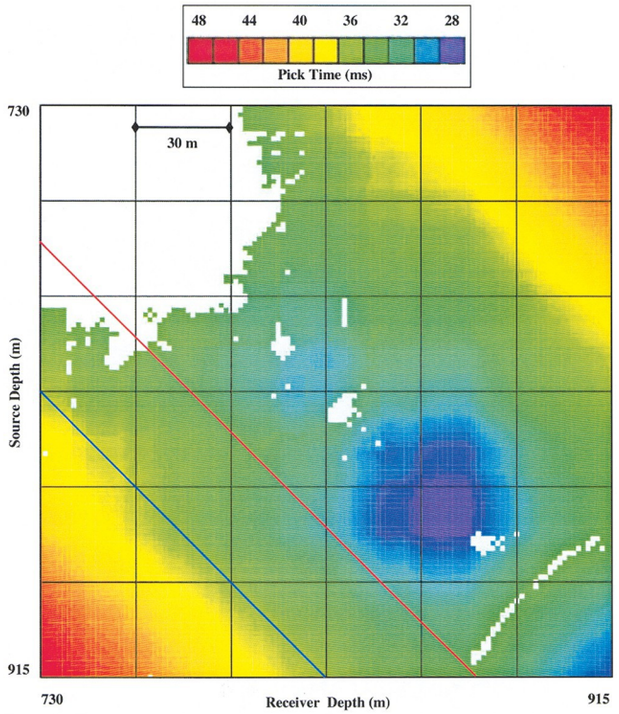

FIG. 6. Traveltime map for the 1-D model finite-difference syn- thetic data. The red line marks the 14° or 45-m offset shown in Figure 7a, the blue line the 28° or 90-m offset shown in Fig- ure 7b. Traveltimes could not be determined for the white area because of waveform complexity.

spacehead-wave arrivals often have very little energy, and waveforms are very complex due to interaction between head waves and other types of arrivals.

2) Consistently determine traveltimes on the direct-arriving energy, develop forward modeling that can generate mul- tivalued arrival times, and select the direct arrival. The same difficulties in estimating traveltimes apply as in (1).
3) Avoid using the offset ranges "contaminated" by wave- form complexity caused by multiple arrivals in the vicinity of Fermat path arrivals.

As noted earlier, we employ the bending method for ray tracing. This makes it very difficult to model direct arrivals in the presence of velocity contrasts that generate head waves because the raypath perturbations we calculate are designed to minimize traveltime. These perturbations lead directly to Fermat paths, or first arrivals, which are head waves in the presence of even moderate velocity contrasts for small offsets. We chose to employ the third alternative for our formulation, and avoid the offset ranges that are contaminated by head- wave energy.

Avoiding multivalued arrivals in the vicinity of the Fermat path arrivals can be accomplished several ways. The simplest method is to exclude certain angle/offset ranges from the data used in the inversion, as was done by Lazaratos and Marion (1997). We call this the "static" or fixed exclusion method. An- other possibility would be to generate rays as usual, and then check for the condition of rays going "postcritical" at each in- terface. Then, any ray determined to be a head wave could be eliminated from the traveltime inversion. This is a "model- based" or dynamic approach to the exclusion of head waves. We first show results achieved by the simple static exclusion of fixed angle/offset ranges in the data, and demonstrate that both vertical and horizontal resolution are degraded by includ- ing the small angles/offsets. Then we examine the model-based approach to excluding head waves and find that the recov- ered vertical spatial bandwidth increases relative to the static method.

In Figure 8, we show the results of including successively more data from small angles/offsets in the inversion. For each of the three examples shown, all parameters controlling the inversion were identical, the only thing changed was the an- gle/offset range included in the inversion. Figure 8a shows the

best tomogram generated by including all angles between 20° and 40°. Figure 8b shows the tomogram for the angle range 10° to 40°, and Figure 8c shows the 0–40° tomogram. For this example, limiting the angles to the range 20–40° gave the best results.

This is confirmed by the model rms difference between each tomogram and the true model. We compute the rms difference after filtering both the tomogram and the true model in the vertical direction with a lowpass Butterworth filter with spatial frequency cutoff 0.667 1/m (wavelength 1.5 m.). The Nyquist spatial frequency for the layer spacing is 0.833 1/m (wavelength 1.2 m). In addition to computing the 2-D model rms, we have also calculated model rms for vertical slices through the tomograms at three locations: at the wells, one-quarter of the distance between wells, and one-half of the distance be- tween wells. These separate vertical slice rms measurements give some indication of horizontal variability for results that would ideally be entirely one dimensional. Table 1 shows these rms values and also includes the number of data (rays) used

space

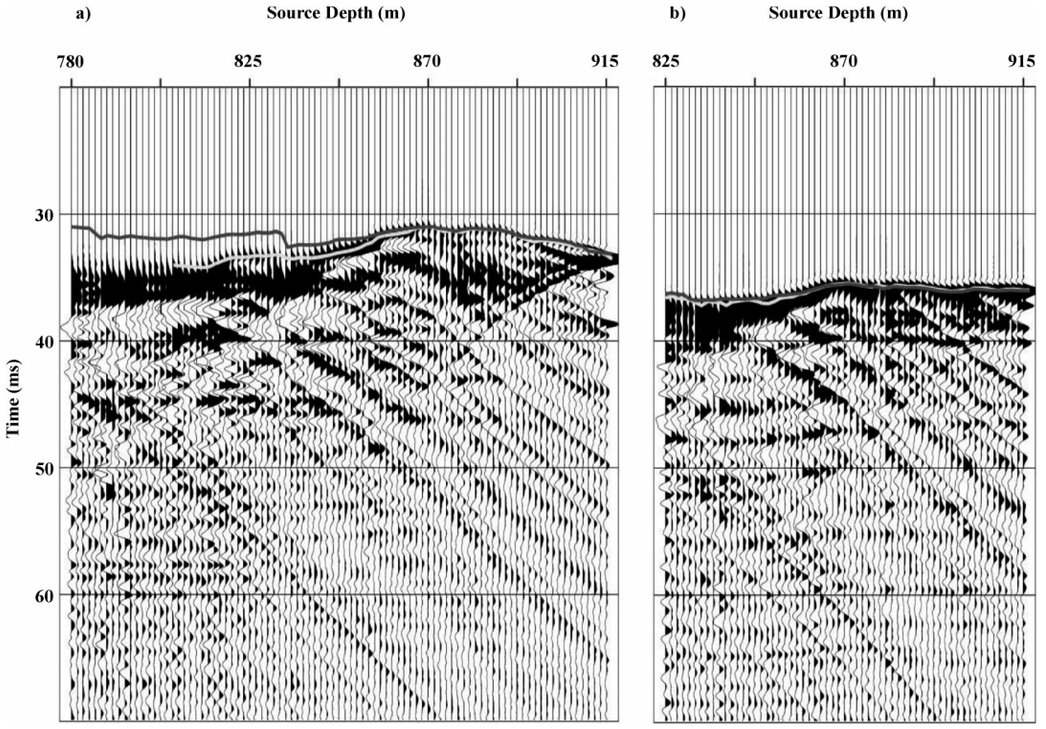

FIG. 7. Two offset gathers from the finite-difference data for the 1-D model shown in Figure 5b: (a) offset=45 m or 14°, (b) offset=0m or 28°. Traveltimes estimated from the data and ray traced in the true model are shown with lines. For the small offsets (a), the difference between ray-traced (upper line) and hand-picked (lower line) traveltimes is clear.

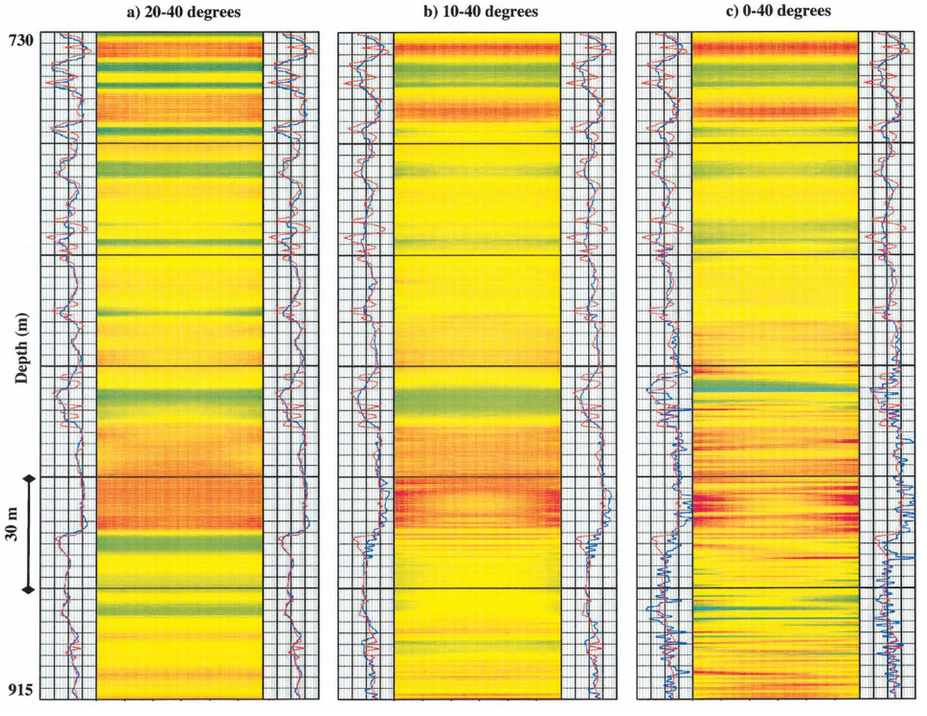

FIG. 8. Comparison of results for static head wave exclusion with various angular apertures: (a) 20–40°, (b) 10–40°, (c) 0–40°. Color scale and log plots as in Figure 5.

spacefor each inversion. Note that in addition to the tomograms shown in Figure 8, Table 1 includes data for two additional angle ranges: 15–40° and 5–40°.

The 2-D rms model mismatch for the 0–40° tomogram (Figure 8c) is 50% higher than for the 20–40° tomogram (Fig- ure 8a). For the tomograms that include the small angles/offsets (Figures 8b and 8c), there is considerably more horizontal variability than for the 20–40° tomogram (Figure 8a). The

Table 1. Number of data points and both 2-D and vertical slice model rms differences from the true model (in meters/second), for various aperture tomograms inverted from the 1-D model synthetic data. Prior to calculation of rms differences, the to- mograms and the true model were Butterworth lowpass spatial filtered to remove wavelengths shorter than 1.5 m (layer spac- ing is 0.6 m).

Aperture (°)	20–40	15–40	10–40	5–40	0–40
Number of data points	5640	7256	8804	10309	11861
2-D rms	352.3	354.4	369.0	471.5	533.1
Vertical rms at wells	353.6	350.9	360.5	459.2	581.6
Vertical rms	350.6	354.1	369.0	471.4	523.1
one-quarter across					
Vertical rms	357.0	361.4	377.0	489.2	539.8
one half across					

spacemaximum variability between the three vertical rms values in Table 1 for the 0–40° tomogram is approximately 10% of the 2-D rms; for the 20–40° tomogram, it is only 2% of the 2-D rms. Although the 0–40° tomogram has nearly twice the data as the 20–40° tomogram (11861 rays compared to 5640 rays), it shows considerably degraded resolution both horizontally and vertically. The fine-scale vertical and horizontal fluctuations evident for the full aperture tomogram (Figure 8c) illustrate the effect of including near offsets or small angles into the traveltime inversion.

For wave-modeled data, we expect both horizontal and ver- tical resolution to degrade away from the wells due to Fresnel zone effects (Williamson and Worthington, 1993; Vasco et al., 1995). However, for our best static head-wave exclusion tomogram (Figure 8a), the combination of the layered parameteri- zation, the horizontal smoothness constraints, and limiting the small angles have overcome the resolution limits imposed by wave behavior. The increased lateral variability in the 0–40° to- mogram (Figure 8c) is evidence that the horizontal smoothness constraints alone do not determine this outcome. The smooth- ness constraints are identical across all panels in Figure 8; thus the constraints are sufficiently weak to allow lateral variability such as in Figure 8c. We therefore conclude that it is primarily the layered parameterization and the exclusion of small an- gles from the inversion that enable consistent resolution as a function of position within the tomogram.

space

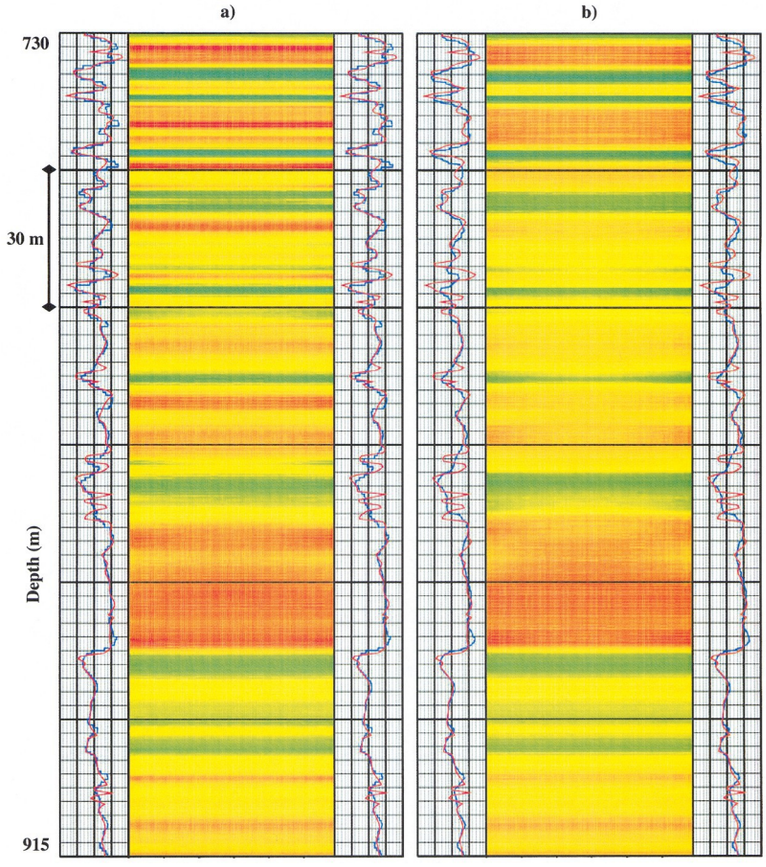

FIG. 9. Best dynamic head-wave exclusion tomogram (a) compared to best static head-wave exclusion tomogram (b) (same as Figure 8a). Color scale and log plots as in Figure 5.

spaceMODEL-BASED EXCLUSION OF HEAD WAVES

The dynamic method for excluding head waves is consider- ably different from the static method of simply limiting certain angle or offset ranges from the inversion. For the model-based method, we begin with a pool of eligible rays (confined to some reasonable angle range, in this case 20–40°). Each ray is a can- didate for the inversion and, after ray tracing, the geometry at each interface is examined to determine if the computed ray has become "postcritical" (incidence angle exceeding crit- ical angle). Any ray found to travel as a head wave (a ray which spends more than a small percentage of its distance con- nected with postcritical refractions) is then excluded from the inversion.

The constant initial velocity model generates straight rays and, for the first iteration, all of the candidate data is used in the inversion. However, as velocity contrasts develop, large numbers of rays can be excluded from the inversion. For the inversion of the 1-D model synthetic data, nearly 75% of rays traced through the final model travel for some distance as head waves and would be discarded from the inversion for the dy- namic approach. Figure 9 compares the final tomogram from inversion of the 1-D model synthetic data using model-based head-wave exclusion (Figure 9a) with the best tomogram from the static head-wave exclusion (Figure 9b, shown previously as Figure 8a). Examination of the log tracks, which plot the true model (red lines) together with the velocities from the edges of the tomogram (blue lines), demonstrate a significantly im- proved fit for the dynamic method relative to the static method. The 2-D rms (307.2 m/s) calculated using the procedure dis- cussed above is improved 13% from the best static result in Table 1.

Figure 10a shows the average vertical amplitude spectra of the two tomograms: the best tomogram for the dynamic head- wave exclusion method (Figure 9a) and the best static method tomogram (Figure 9b). "Best" here refers to the tomogram with the smallest rms difference from the true model after ap- plying the vertical lowpass filter as above. Vertical amplitude spectra for Figure 10a are calculated after averaging over hor- izontal position. A three-point running average filter was also applied to the amplitude spectra. Figure 10a shows that the ver- tical bandwidth is considerably higher for the dynamic model- based approach to excluding head waves. Moreover, the lower rms error for the model-based approach indicates that this in- creased vertical frequency content is an improvement in signal, not noise.

The percentage of rays that travel as head waves is related to the "roughness" of the model. In order to quantify model roughness, we use the equivalent width of the amplitude spec- tra (after Bracewell, 1978). The equivalent width of a strictly positive function like an amplitude spectrum is defined as the width of a boxcar of the same area having the same peak value. To calculate equivalent width for the tomogram ver- tical wavenumber spectrum, we integrate amplitude over fre- quency and then divide by the peak amplitude (for tomograms this is the dc component at zero frequency). Figure 10b plots the percentage of rays that travel for part of the interwell dis- tance as head waves versus the equivalent width of the av- erage vertical wavenumber spectrum of the interwell velocity field as the inversion proceeds. Also shown is the 2-D model rms (computed as described above) for the complete nonlin- ear iterations used to generate Figure 9 (both for the dynamic spaceand static head-wave exclusion methods). Figure 10b illus- trates that, for this 1-D model, the percentage of head waves generated is proportional to our equivalent width measure of model roughness. The fractions of data shown as head waves in Figure 10b were discarded from the inversion to generate Figure 9a.

For our model-based head-wave exclusion approach, we lose the ability to monitor the data error term as in con- ventional tomography. We no longer have a stable set of data from which to generate an error norm that is consistent across iterations. However, it is also very important to recog- nize that the fundamental consistency of the dataset (travel- times corresponding to energy propagating as waves) and the forward modeling (traveltimes from ray theory appropriate for high-frequency energy propagation) deteriorates with in- creasing model roughness because the forward modeling will increasingly propagate rays as head waves. Continuing to in- clude data whose associated forward modeling is increasingly inconsistent will lead to artifacts in tomograms. For an ap- proach to regularization such as the continuation strategy, this is particularly problematic because the increasing inconsis- tency of the data and the forward modeling will in general

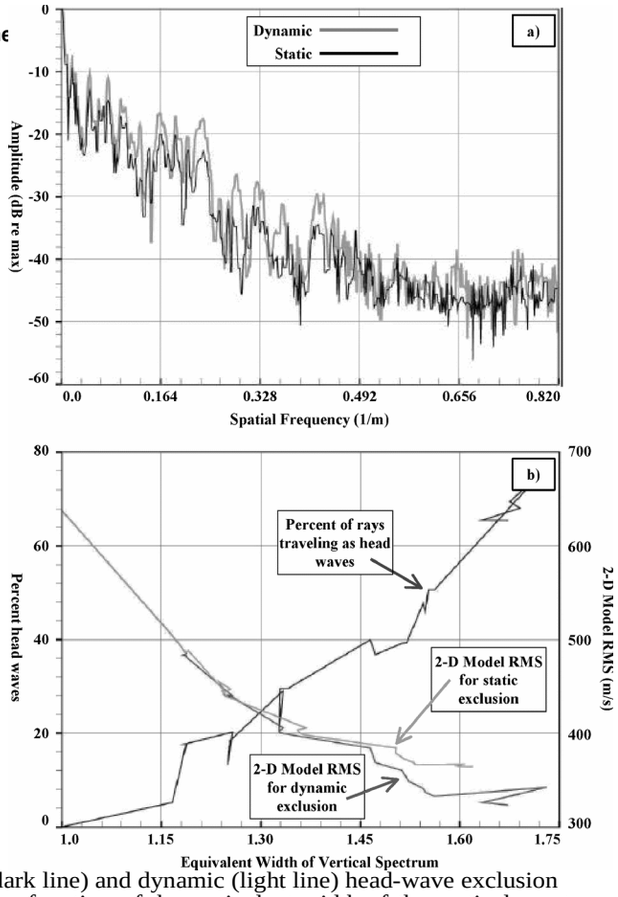

FIG. 10. (a) Vertical bandwidth of best tomograms for the static (dark line) and dynamic (light line) head-wave exclusion meth- ods, and (b) percentage of rays traveling as head waves as a function of the equivalent width of the vertical spectrum, and 2-D model rms for both the dynamic method and the static method of head-wave exclusion.

spacebe inversely proportional to the level of applied smoothing constraints.

Figure 10b also shows the model rms as a function of the equivalent width of vertical wavenumber spectrum for both head-wave exclusion approaches. The static method neither reaches as small a 2-D model rms nor achieves the same level of model roughness as the dynamic method. By excluding the increasing number of head waves (as the iterative inversion proceeds), the dynamic method is able to recover more vertical bandwidth and achieve the smaller model residuals.

DEMONSTRATION OF THE CONTINUATION STRATEGY

In Figure 11, we illustrate the continuation approach for the synthetic data discussed above. In the figure, the values of the tomogram at both edges of the model are plotted like logs for comparison with the true model. The tomogram values are shown in blue, the true velocity values are shown in red. Start- ing from a constant initial velocity (usually the average velocity for all included rays), we show the first, third, and fifth "contin- uation steps." The true model is one dimensional; thus, we are interested in vertical resolution. The first continuation steps resolve the lowest frequency components, and successive con- tinuation steps resolve successively higher frequency parts of the model. The regularization parameters for vertical and hor- izontal smoothness are decreased by a factor of 10 at the end of each continuation step (determined empirically to give rea- sonable convergence rates while not changing the problem a great deal between successive continuation steps).

spaceBy successively solving a series of five fixed regularization problems, we have decreased the constraints by two orders of magnitude from their initial level. However, if we start the pro- cess with the regularization level used in the fifth continuation step, the model quickly diverges (see Bube and Langan, 1994, 1999). Figure 12 shows the results of starting the inversion, again from the same constant initial average velocity, and using fixed regularization at the level equivalent to the fifth contin- uation step. In this figure, the tomogram from the fifth contin- uation step—shown previously in Figure 11c—is included as Figure 12b for comparison.

VERTICAL AND HORIZONTAL RESOLUTION

The choice of model parameterization for the crosswell traveltime tomography problem effectively controls the tradeoff between vertical resolution and lateral resolution (Goudswaard et al., 1998). Our choice to use Chebyshev poly- nomials to represent horizontal structure limits the ability to resolve lateral variations. One can select an appropriate model parameterization enabling higher lateral resolution at the cost of degraded vertical resolution. Goudswaard et al. (1998) use a parameterization that fixes vertical structure and allows lateral variation, and is therefore able to resolve effectively the lateral position of a vertical fault between wells.

We have chosen to improve vertical resolution at the cost of horizontal resolution; therefore, the lateral resolution for the fault model is poor. Figure 13 shows the best tomogram for the synthetic data generated from the fault model. Here, best refers

space

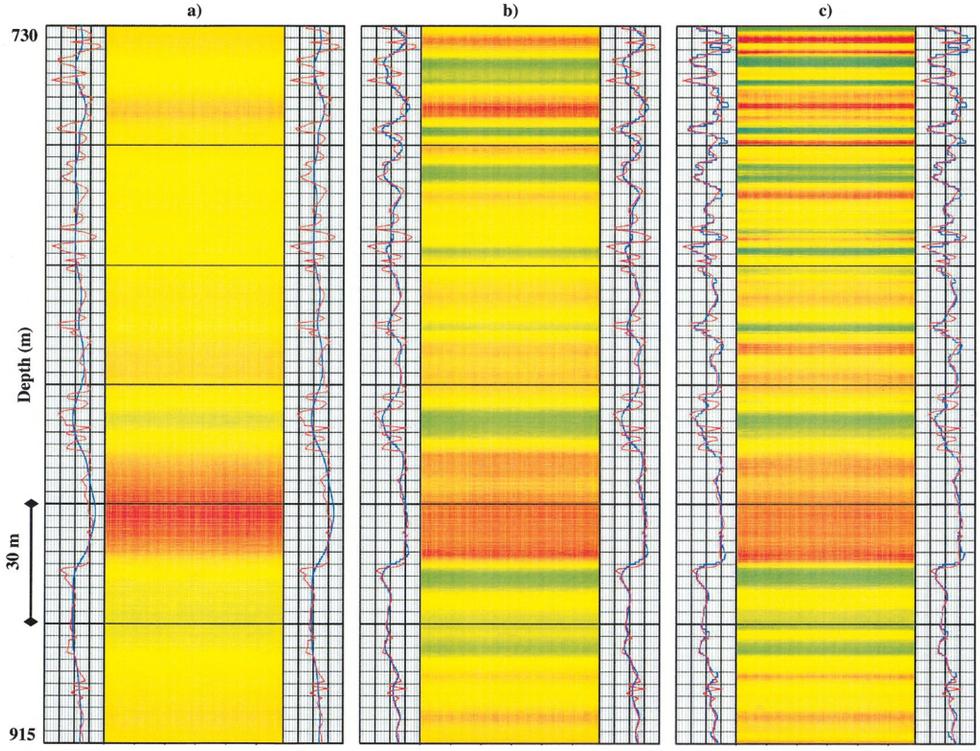

FIG. 11. Tomograms illustrating the continuation approach: (a) one continuation step, (b) three continuation steps, and (c) five continuation steps. Color scale and log plots as in Figure 5.

spaceto the tomogram with the smallest filtered 2-D rms difference from the true model. Vertical bandwidth suffers compared to the best result for the 1-D model because of the contribution from rms difference in the faulted area of the model. Figure 13 also shows the true model for comparison. The inversion does a reasonable job recovering a smoothed lateral variation cen- tered at the fault.

SIMULTANEOUS INVERSION OF MULTIPLE-PROFILE CROSSWELL DATA: REAL DATA EXAMPLE

One advantage of the model parameterization discussed above is that the data from multiple crosswell profiles can be used simultaneously to resolve a single 3-D velocity distribu- tion. This ability is demonstrated on multiple crosswell sur- veys collected in Chevron's Cymric field, located in the San Joaquin Valley, California. At Cymric, the reservoir rock is high-porosity, low-permeability siliceous shale, and to produce the heavy oils from the formation usually requires enhanced oil recovery processes such as steam injection (Langan et al., 1999). The goal of the crosswell surveys was to monitor (in three dimensions) the steam movement.

In the survey area (a region roughly 50 r×50 m), there are four significantly deviated wells: an injector well, not used for the crosswell survey, and three temperature observation (TO)

spacewells. The wells occupy the limb of an anticline, and there is significant structural dip in the area, ranging to as high as 70°. The steep dips combined with the deviated wells make it very challenging to image the profiles successfully using traditional 2-D crosswell technology.

Four snapshots between two crosswell profiles were acquired between May 1997 and May 1998. Elevation and plan views of the four wells are shown in Figure 14. Figure 14a shows the horizon picks from wireline log correlations and the Cheby- shev polynomial surfaces fit to them. In Figure 14b, each arrow indicates a crosswell profile with the point of the arrow at the receiver well. The figure also shows a map view of the well tra- jectories over the acquisition depth range of 213 to 426 m, with the top of this zone marked by a cross. The wells are very close together, with the average profile distances over the depth in- terval logged 27 (TO4 TO2) and 21 (TO4 TO3) m.

The Cymric Pilot Project used cyclic steam injection to en- hance oil recovery. Several days of high-pressure injection are followed by month-long periods during which reservoir pressure is depleted by production. Laboratory measurements made at Chevron indicate that both increasing steam sat- uration and increasing temperature result in lower seismic velocities for Cymric reservoir rock (Langan et al., 1999). Al- though we are unable to separate these effects, we can im- age the combined result with 3-D traveltime tomography. The →

space

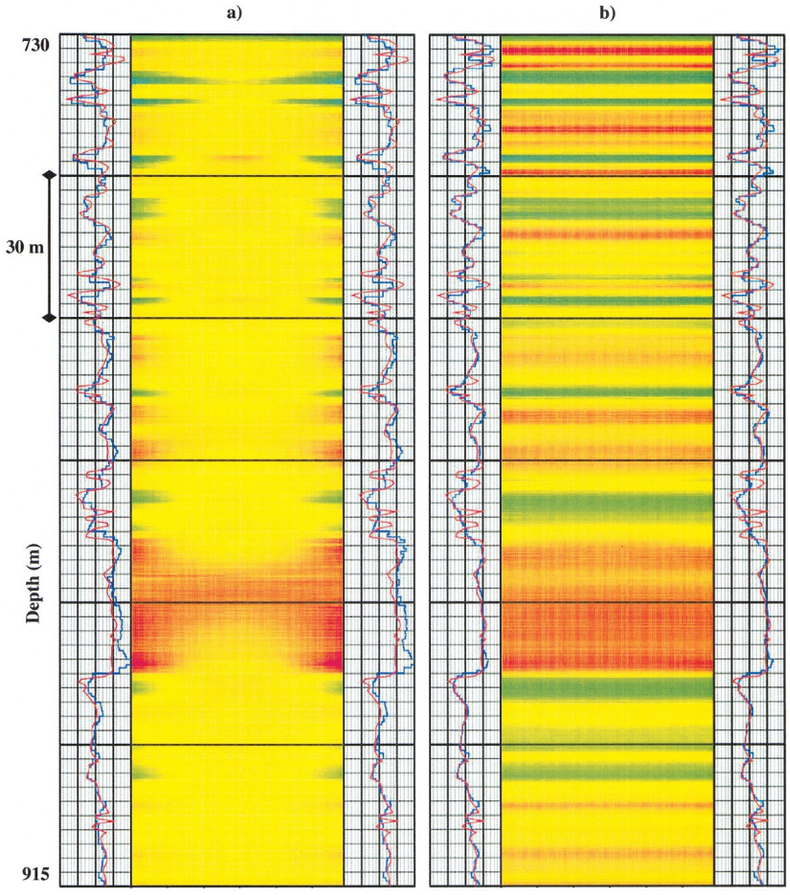

FIG. 12. Comparison of (a) tomogram using fixed regularization with (b) tomogram from the fifth continuation step. Regularization level is equivalent for both tomograms. Color scale and log plots as in Figure 5.

spacefirst crosswell snapshot (May 1997) was acquired at the end of the production phase of the fifth cycle, with reservoir pres- sure depleted. The second snapshot (August 1997) occurred during the injection phase of the seventh cycle. The last two snapshots were acquired several cycles later, at the end of an injection phase (April 1998) and about two weeks into the fol- lowing production phase (May 1998). From analysis of this pressure data, we expect the combined effects of tempera- ture and steam—seismically evident as reduced velocities in the vicinity of the injector well—to be small for the first survey, building for the second survey, most noticeable for the third survey, and somewhat reduced but still evident for the final snapshot.

Figure 15 shows constant depth slices (*XY* planes) through the 3-D tomograms from each of the four time snapshots. This type of areal resolution is impossible for conventional 2-D tomography without some method of interpolation/ extrapolation between wells. The 3-D tomograms resolve the low-velocity trend appearing in the later snapshots (particu- larly the last two) as well defined and clearly surrounding the injector well (marked "INJ" in the figure). The velocity color scale shows the slowest velocities (1,067 m/s) as dark blues, and the highest velocities (2,743 m/s) as reds. We believe that the significant changes in character between the second and third time snapshots are due to the combined effects of steam satu-

spaceration and temperature increase in the vicinity of the injector well. The *XY* planes shown in Figure 15 are from a depth of 330 m. This correlates very well with the approximate depth of the perforations in the injector well (325–350 m). Again, this type of result can not be generated by conventional 2-D meth- ods, and reflects one of the more significant advantages of a fully 3-D model parameterization.

In Figure 16, we compare the results from the simultaneously processed 3-D multiple-profile inversion with results from the independently processed single-profile inversions. The tomo- grams are plotted as "sections" to illustrate the nature of the velocity tie between the two profiles at the common well. The independently processed single profiles (Figure 16b) and the simultaneously processed multiple profiles (Figure 16a) are quite similar in character. The main effect of performing multi- ple profile inversion is to smooth the tomograms slightly in the vertical direction and to guarantee the tie across the common well. We believe that the vertical smoothing is due to slight depth statics between the two profiles at the common well that do not affect the single profile results.

CONCLUSIONS

We have presented a 3-D model formulation and inver- sion strategy for crosswell direct arrival traveltimes capable of space

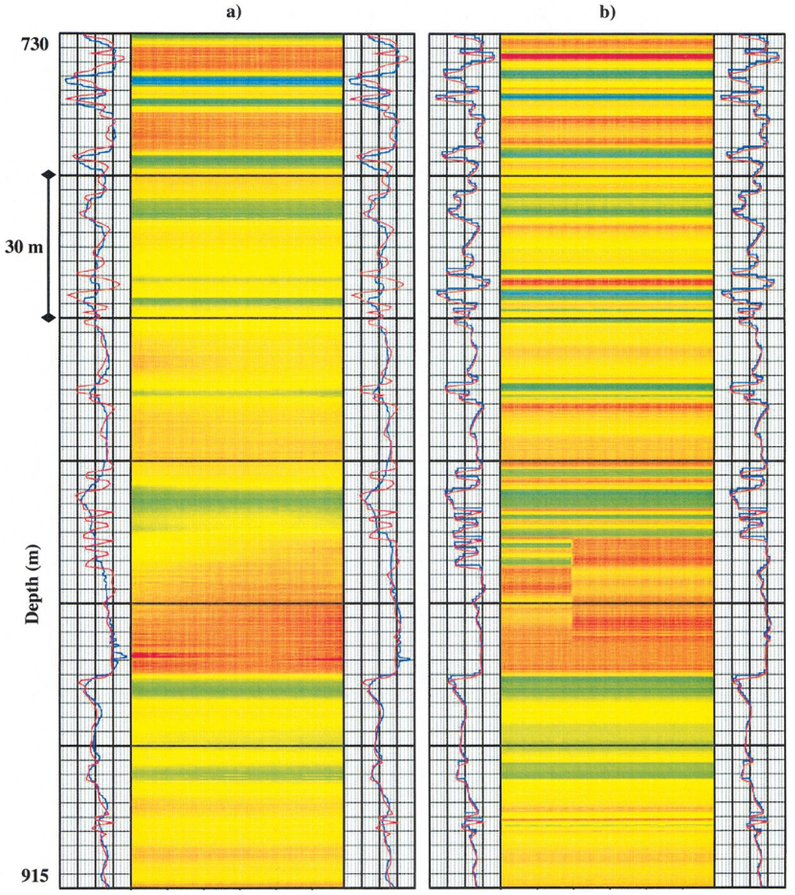

FIG. 13. Results from the fault model: (a) best tomogram and (b) true model. Color scale and log plots as in Figure 5.

spacehandling well deviations and multiple-profile crosswell data- sets. We obtain high vertical resolution, comparable to the vertical resolution of wireline logs. By comparison, traveltime tomography performed using conventional pixelized models with the maximum aperture available in the data may produce results with much lower vertical resolution.

The key idea is to parameterize the model as thinly layered and vertically discontinuous, with few degrees of freedom later- ally in each layer. We use a simple Chebyshev polynomial rep- resentation for surfaces and the velocities between surfaces, re- sulting in many fewer parameters than required for traditional pixelized models. We have also incorporated a continuation strategy to smoothing constraints, which maximizes the contri- bution of data to the solution, and minimizes the "overprint" of regularization.

A second major idea contributing to high vertical resolu- tion is the limitation of certain angles/offsets in the inversion

spacethat correspond to raypaths traveling nearly parallel to geo- logic layering. These raypaths are not required for high verti- cal resolution when the model is parameterized with horizontal layers.

We used two methods for the exclusion of head waves from traveltime inversion: a static approach that limits a fixed range of angles/offsets, and a model-based approach where any ray determined to travel as a head wave is excluded. For the static method, the angle range of 20–40° (with respect to layer interfaces) produces the best results for a synthetic wave- modeled dataset. Including smaller angles/offsets in the inver- sion degrades both the vertical and the lateral resolution of the tomograms because the traveltimes determined for these angles/offsets are often inconsistent with the ray theory upon which the tomography is based. Using the model-based ap- proach to exclude head waves results in a tomogram with con- siderably broader vertical bandwidth and smaller model rms.

space

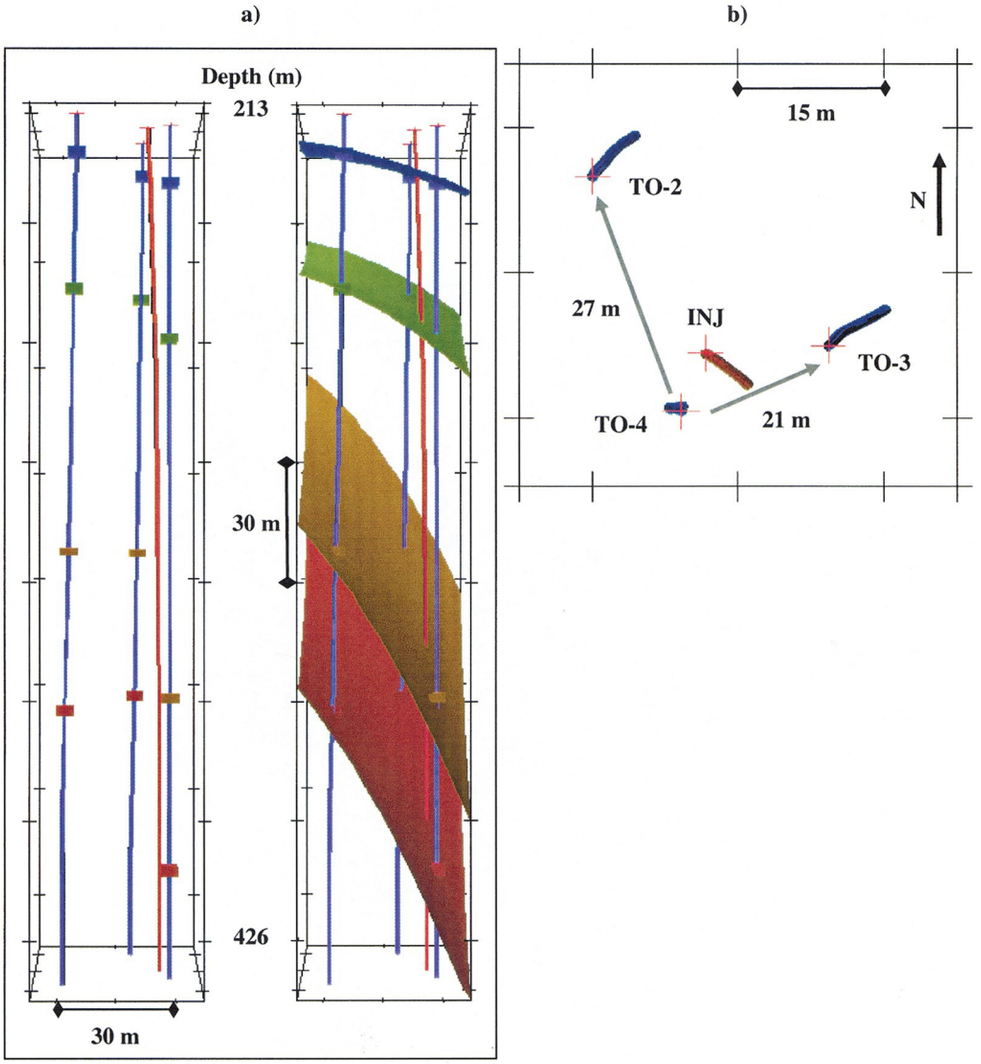

FIG. 14. Cymric crosswell geometry: (a) elevation view of wells, horizon picks, and surfaces fit to horizon picks; (b) map view showing well trajectories over the depth interval of the crosswell survey (temperature observation wells are marked TO, and the injector well is marked INJ).

space

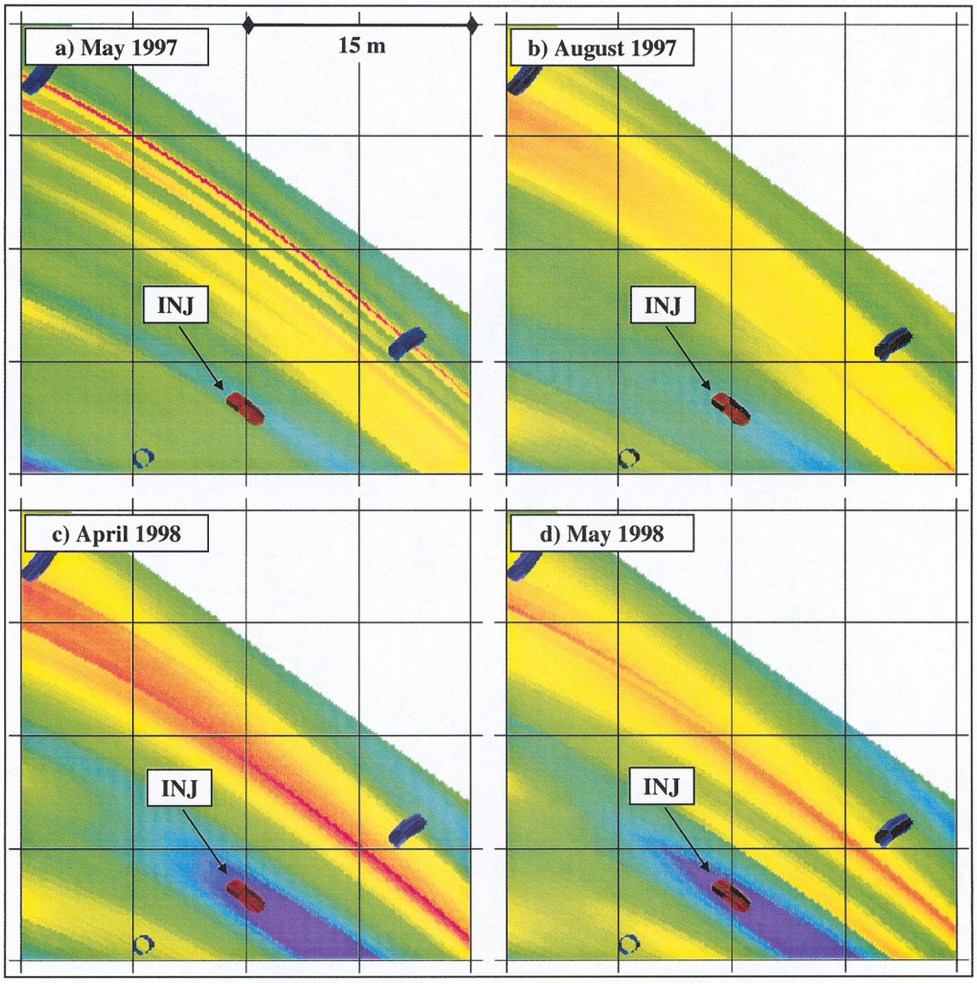

FIG. 15. Depth slices at 330 m through the four snapshot 3-D tomograms. Color scale as in Figure 16; wells are marked as in Figure 14.

space For the static approach—and by extension any conventional tomography—the increasing inconsistency between the data and the forward modeling with increasing model roughness does not allow resolution of the vertical bandwidth required for smaller model residuals.

A key advantage of our 3-D model parameterization is that we can model crosswell datasets from areas of steep structural dips and/or significant well trajectory deviations. We are able to apply the data from multiple crosswell profiles simultaneously to the resolution of a single 3-D velocity distribution.

ACKNOWLEDGMENTS

The authors gratefully acknowledge Spyros Lazaratos and Bruce Marion for invaluable insight in the development of our model parameterization, and Robert Langan, Dale Julander, Fred Bair, and Scott Johnson of Chevron for release of the Cymric data. The authors also thank Reinaldo Michelena and an anonymous reviewer for their helpful comments. Funding for this research came in part from a Department of Energy Phase II Small Business Innovation Research (SBIR) Grant.

space**REFERENCES**

Bracewell, R. N., 1978, The Fourier transform and its applications: McGraw Hill Book Co.
Bregman, N. D., Bailey, R. C., and Chapman, C. H., 1989, Crosshole seismic tomography: Geophysics, **54**, 200–215.
Bube, K. P., and Langan, R. T., 1994, A continuation approach to regularization for traveltime tomography: 64th Ann. Internat. Mtg., Soc. Expl. Geophys., Expanded Abstracts, 980–983.
——— 1997, Hybrid l^1/l^2 minimization with applications to tomogra- phy: Geophysics, **62**, 1183–1195.
——— 1999, On a continuation approach to regularization for cross-well tomography: 69th Ann. Internat. Mtg., Soc. Expl. Geophys., Expanded Abstracts, 1295–1298.
Bube, K. P., and Meadows, M. A., 1998, Characterization of the null space of a generally anisotropic medium in linearized cross-well to- mography: Geophys. J. Internat., **133**, 65–84.
Carrion, P., Persoglia, S., and Poletto, F., 1995, High resolution travel- time imaging: The Leading Edge, **14**, 26–28.
Chapman, C. H., and Pratt, R. G., 1992, Traveltime tomography in anisotropic media—I. Theory: Geophys. J. Internat., **109**, 1–19.
Chiu, S. K. L., Kanasewich, E. R., and Phadke, S., 1986, Three-dimensional determination of structure and velocity by seismic to- mography: Geophysics, **51**, 1559–1571.
Chiu, S. K. L., and Stewart, R. R., 1987, Tomographic determination of three-dimensional seismic velocity structure using well logs, vertical seismic profiles, and surface seismic data: Geophysics, **52**, 1085–1098.
Dines, K. A., and Lytle, R. J., 1979, Computerized geophysical tomography: Proc. IEEE, **67**, 1065–1073.

space

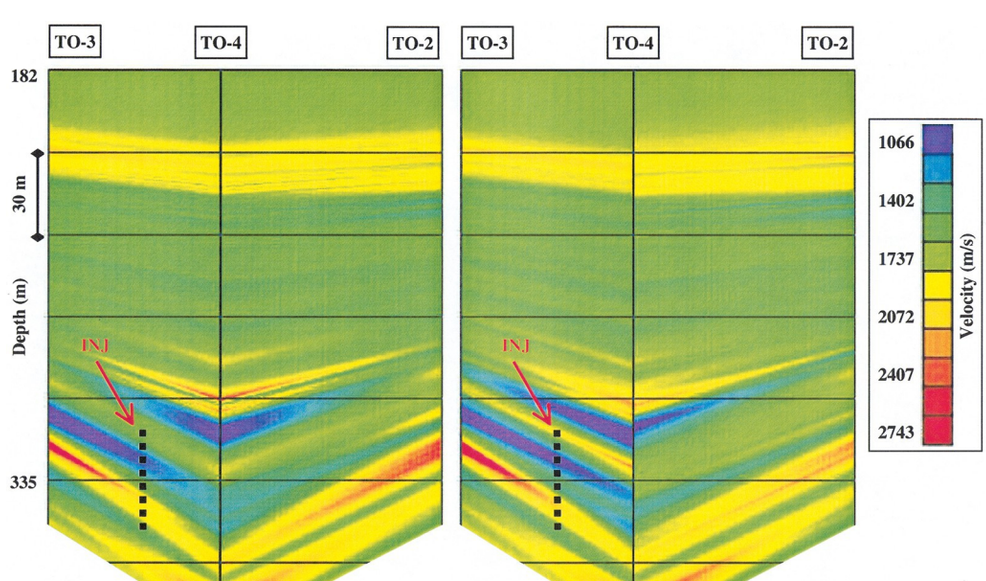

FIG. 16. Cymric tomogram section plots: (a) 2-D slices of the simultaneously processed 3-D multiple profile, and (b) independently processed single profiles. The black broken line shows the approximate location of the injector. Wells are marked as in Figure 14.

spaceEttrich, N., and Gajewski, D., 1998, Traveltime computation by pertur- bation with FD-eikonal solvers in isotropic and weakly anisotropic media: Geophysics, **63**, 1066–1078.

Eppstein, M. J., and Dougherty, D. E., 1998a, Optimal 3D traveltime tomography: Geophysics, **63**, 1053–1061.

——— 1998b, Efficient three-dimensional data inversion: Soil characterization and moisture monitoring from cross-well ground- penetrating radar at a Vermont test site: Water Res. Bull., **34**, 1889– 1900.

Goudswaard, J. C. M., ten Kroode, F. P. E., Snieder, R. K., and Verdel, A. R., 1998, Detection of lateral velocity contrasts by crosswell trav- eltime tomography: Geophysics, **63**, 523–533.

Grechka, V. Y., and McMechan, G. A., 1996, 3D two-point ray tracing for heterogeneous, weakly transversely isotropic media: Geophysics, **61**, 1883–1894.

Guiziou, J. L., Mallet, J. L., and Madariaga, R., 1996, 3D seismic reflec- tion tomography on top of the GOCAD depth modeler: Geophysics, **61**, 1499–1510.

Harris, J. M., Nolen-Hoeksema, R. C., Langan, R. T., Van Schaack, M., Lazaratos, S. K., and Rector, J. W. III., 1995, High- resolution crosswell imaging of a west Texas carbonate reservoir: Part 1—Project summary and interpretation: Geophysics, **60**, 667–681.

Hyndman, D. W., and Harris, J. M., 1996, Traveltime inversion for the geometry of aquifer lithologies: Geophysics, **61**, 1728–1737.

Jervis, M., Addington, C., Washbourne, J., Malcotti, H., Capello, M., and Vasquez, M., 2000, High-resolution crosswell reflection imaging in the presence of anisotropy: The Santa Rosa gas field, eastern Venezuela: 70th Ann. Internat. Mtg., Soc. of Expl. Geophys., 1631– 1635.

Julian, B. R., and Gubbins, D., 1977, Three-dimensional seismic ray tracing: J. Geophys., **43**, 95–113.

Kelly, K. R., Ward, R. W., Treitel, S., and Alford, R. M., 1976, Syn- thetic seismograms: A finite-difference approach: Geophysics, **41**, 2–27.

Langan, R. T., Lerche, I., and Cutler, R. T., 1985, Tracing of rays through heterogeneous media: An accurate and efficient procedure: Geophysics, **50**, 1456–1465.

Langan, R. T., Morea, M. F., Lazaratos, S. K., Julander, D., and Adding- ton, C., 1998, Crosswell seismic imaging in the Buena Vista Hills, San Joaquin Valley: A case history: 68th Ann. Internat. Mtg., Soc. Expl. Geophys., Expanded Abstracts, 353–356.

Langan, R., Washbourne, J., Bair, F., Johnson, S., Julander, D., and Meyer, J., 1999, Time-lapse imaging of steam and heat movement in the Cymric 36W Cyclic Steam Pilot using crosswell seismology:

spaceSEG 69th Ann. Internat. Mtg., Soc. Expl. Geophys., Expanded Abstracts, 1643–1646.

Lazaratos, S., and Marion, B., 1997, Crosswell seismic imaging of reser- voir changes caused by CO_2 injection: The Leading Edge, **16**, 1300– 1308.

Luo, Y., and Schuster, G. T., 1991, Wave-equation traveltime inversion: Geophysics, **56**, 645–653.

Meyerholtz, K. A., Pavlis, G. L., and Szpakowski, S. A., 1989, Convo- lutional quelling in seismic tomography: Geophysics, **54**, 570–580.

Michelena, R. J., 1993, Singular value decomposition for cross-well tomography: Geophysics, **58**, 1655–1661.

Michelena, R. J., and Harris, J. M., 1991, Tomographic traveltime in- version using natural pixels: Geophysics, **56**, 635–644.

Michelena, R. J., Harris, J. M., and Muir, F., 1995, Crosswell tomographic estimation of elastic constants in heterogeneous transversely isotropic media: Geophysics, **60**, 774–783.

Michelena, R. J., Muir, F., and Harris, J. M., 1993. Anisotropic travel- time tomography: Geophys. Prosp., **41**, 381–412.

Nemeth, T., Normark, E., and Qin, F., 1997, Dynamic smoothing in crosswell traveltime tomography: Geophysics, **62**, 168–176.

Peterson, J. E., and Davey, A., 1991, Crossvalidation method for cross- well seismic tomography: Geophysics, **56**, 385–389.

Phillips, W. S., and Fehler, M.C., 1991, Traveltime tomography: A com- parison of popular methods: Geophysics, **56**, 1639–1649.

Pilkington, M., and Todoeschuck, J. P., 1991, Naturally smooth inver- sions with a priori information from well logs: Geophysics, **56**, 1811– 1818.

Pratt, R. G., and Chapman, C. H., 1992. Traveltime tomography in anisotropic media—II. Application: Geophys. J. Internat., **109**, 20–37.

Rector, J. W. III., and Washbourne, J., 1994, Characterization of res- olution and uniqueness in crosswell direct arrival traveltime tomography using the Fourier projection slice theorem: Geophysics, **59**, 1642–1649.

Saito, H., 1991, Anisotropic traveltime tomography at the Buckhorn Test Facility in Illinois: 61st Ann. Internat. Mtg., Soc. Expl. Geophys., Expanded Abstracts, 123–126.

Scales, J. A., 1987, Tomographic inversion via the conjugate gradient method: Geophysics, **52**, 179–185.

Scales, J. A., and Gersztenkorn, A., 1988, Fast l_p solution of large, sparse, linear systems: Applications to seismic travel time tomogra- phy: J. Comp. Phys., **75**, 314–333.

Squires, L., and Cambois, G., 1992, A linear filter approach to designing off-diagonal damping matrices for least-squares inverse problems: Geophysics, **57**, 948–951.

space

Squires, L. J., Stoffa, P. L., and Cambois, G., 1994, Borehole trans- mission tomography for velocity plus statics: Geophysics, **59**, 1028– 1036.

Tikhonov, A. N., and Arsenin, V. Y., 1977, Solutions of ill-posed prob- lems: V. H. Winston and Sons.

Vasco, D. W., Peterson, J. E., and Majer, E. L., 1995, Beyond ray tomo- graphy: Wavepaths and Fresnel volumes: Geophysics, **60**, 1790–1804. Vidale, J. E., 1988, Finite-difference calculation of traveltimes: Bull.

Seis. Soc. Am., **78**, 2062–2076.
Virieux, J., and Farra, V., 1991, Ray tracing in 3D complex isotropic media: Analysis of the problem: Geophysics, **56**, 2057– 2069.
Washbourne, J., Jervis, M., Malcotti, H., and Capello, M., 2000, Evi- dence of anisotropy from 3D crosswell tomography in a giant gas space
field, Venezuela: 70th Ann. Internat. Mtg., Soc. Expl. Geophys., Ex- panded Abstracts, 586–589.
Williamson, P. R., 1990, Tomographic inversion of reflection seismol- ogy: Geophys. J. Internat., **100**, 255–274.
——— 1993a, Anisotropic crosshole tomography in layered media, Part I: Introduction and methods: J. Seis. Expl., **2**, 107–121.
——— 1993b, Anisotropic crosshole tomography in layered media, Part II: Applications, results, and conclusions: J. Seis. Expl., **2**, 223– 238.
Williamson, P. R., and Worthington, M. H., 1993, Resolution limits
in ray tomography due to wave behavior: Numerical experiments: Geophysics, **58**, 727–735.
Woodward, M. J., 1992, Wave-equation tomography: Geophysics, **57**,
15–26.

APPENDIX A

CALCULATION OF TRAVELTIME AND LINEAR SYSTEM OF EQUATIONS USED FOR RAY TRACING

Parametric traveltime calculation

The line integrals for traveltime in our model are calculated using Chebyshev polynomials and the traveltime within a single layer are repeated here from equations (1) and (2):

$$S(x, y) = C_0 + C_1x + C_2y + C_3xy + C_4(2x^2 - 1) + C_5(2y^2 - 1) + C_6(2x^3 - 3x) + C_7(2y^3 - 3y) + C_8(4x^3 - 3x) + C_9(4y^3 - 3y), \quad \text{(A-1)}$$

$$t = \int_A^B S(x, y)\,dl. \quad \text{(A-2)}$$

Here, C_0 through C_9 are the polynomial coefficients, and A and B have the coordinates (x_1, y_1, z_1) and (x_2, y_2, z_2), according to Figure 4. First, we express x, y, and z in parametric form:

$$x = x_1 + \sigma\delta x \quad \delta x = (x_2 - x_1),$$

$$y = y_1 + \sigma\delta y \quad \delta y = (y_2 - y_1), \quad \text{(A-3)}$$

$$z = z_1 + \sigma\delta z \quad \delta z = (z_2 - z_1),$$

$$dl = (\delta x^2 + \delta y^2 + \delta z^2)^{1/2} d\sigma = [\sigma(\delta x^2 + \delta y^2 + \delta z^2)]^{1/2}, \quad \text{(A-5)}$$

$$t = \int_0^1 S(\sigma)\,d\sigma. \quad \text{(A-6)}$$

Finally, after integration over σ, the traveltime within a single layer becomes

$$t = \frac{1}{2}\sqrt{(x_2 - x_1)^2 + (y_2 - y_1)^2 + (z_2 - z_1)^2}\,\{C_1(x_1 + x_2) + C_2(y_1 + y_2) + 2C_3(x_1 + x_2)(y_1 + y_2) + 2C_4[(x_1 + x_2)^2 - 2] + 2C_5[(y_1 + y_2)^2 - 2] + C_6[(x_1 + x_2)^3 - 3(x_1 + x_2)] + C_7[(y_1 + y_2)^3 - 3(y_1 + y_2)] + C_8[(x_1 + x_2)^4 - 4(x_1 + x_2)^2 + 3] + C_9[(y_1 + y_2)^4 - 4(y_1 + y_2)^2 + 3]\}.$$

$$z = z_1 + \sigma\delta z \qquad \delta z = (z_2 - z_1)$$

$$+ C_3 \left[\frac{1}{3}(x_1 y_1 + x_2 y_2) + \frac{1}{6}(x_1 y_2 + x_2 y_1)\right]$$

The parameter σ ranges from 0 to 1, and by substitution we can replace equation (A-1) with one that involves only σ and the constants (x, y, δx, δy):

$$+ C \left[\frac{2}{2}(x^2 + x\,x + x^2) - 1\right]$$

$$S(\sigma) = C_0 + C_1[\sigma\delta x + x_1] + C_2[\sigma\delta y + y_1]$$
$$+ C_5 \left[\frac{1}{3}(y_1 + y_1 y_2 + y_2) - 1\right]$$
$$+ C_3 \left[\sigma^2\delta x\delta y + x_1\sigma\delta y + y_1\sigma\delta x + x_1 y_1\right]$$

$$+ C \left[\frac{1}{2}x^2 y + \frac{1}{2}x^2 y + \frac{1}{2}(x\,x\,y + x\,x\,y)\right]$$

$$+ C_4 \left[2\sigma^2\delta x^2 + 4x_1\sigma\delta x + 2x^2 - 1\right]$$
$$+ C_5 \left[2\sigma^2\delta y^2 + 4y_1\sigma\delta y + 2y^2 - 1\right]$$
$$+ \left[\frac{1}{6}(x_2 y_1 + x_2 y_2) - \frac{1}{2}(y_1 + y_2)\right]$$

$$+ C_6 \left[2\sigma^3\delta x^2\delta y + 4x_1\sigma^2\delta x\delta y + 2x^2\sigma\delta y\right]$$

$$+ C \left[\frac{1}{2}y^2 x + \frac{1}{2}y^2 x + \frac{1}{2}(y\,y\,x + y\,y\,x)\right]$$
$$+ 2y_1\sigma^2\delta x^2 + 4x_1 y_1\sigma\delta x + \sigma\delta y + 2x^2 y_1 + y_1$$
$$+ C_7 \left[2\sigma^3\delta y^2\delta x + 4y_1\sigma^2\delta y\delta x + 2y^2\sigma\delta x\right]$$
$$+ \left[\frac{1}{6}(y_2 x_1 + y_2 x_2) - \frac{1}{2}(x_1 + x_2)\right]$$

$$+ 2x_1\sigma^2\delta y^2 + 4y_1 x_1\sigma\delta y + \sigma\delta x + 2y^2 x_1 + x_1$$

$$+ C \left[x^3 + x^3 + x^2 x + x\,x^2 - \frac{1}{3}(x + x)\right]$$

$$+ C_8 \left[4\sigma^3\delta x^3 + 12x_1\sigma^2\delta x^2 + 12x^2\sigma\delta x + 3\sigma\delta x\right]$$

$$+ C_9 \left[4\sigma^3\delta y^3 + 12y_1\sigma^2\delta y^2 + 3y_1 + 4y^3\right]. \qquad \text{(A-4)}$$

The variable $\mathcal{L}$ is the length along the straight-line segment of the ray, and we find the required change of variable to the parameter σ for the integral:

We can observe from the form of this equation that partial derivatives of traveltime can be calculated in closed form. In particular the derivatives with respect to the ten slowness

spacecoefficients, used for the velocity inversion, are very simple to determine.

For a ray that passes through n layers, the total traveltime is then

$$T = \sum_{i=1}^{n} t_i. \qquad \text{(A-8)}$$

The linear system of equations d for ray tracing

As described earlier, ray tracing is performed via the bending method. We can take advantage of the structural stratification of the model, and treat z as a function of x and y on each of the surfaces that a ray intersects. We then only need to solve for updates to x and y at each surface. For each ray, we first organize the x and y intersections for the n layers the ray passes through into a vector of length $2n$:

$$X = (x_1, y_1, x_2, y_2, \ldots, x_n, y_n). \qquad \text{(A-9)}$$

We solve the minimization problem by using Newton's method to find the critical points of the objective function. In each iteration, we have the following linear system:

spacewith respect to elements of X more than two indices apart is zero. The Hessian matrix of second derivatives of traveltime is therefore symmetric and band-diagonal, with nonzero ele- ments in only three super-diagonals. Table A-1 shows the form of the Hessian. For the derivatives with respect to the inter- section of the ray with the i th layer, only the seven elements within the dashed lines in Table A-1 need to be calculated.

Table A-1. Hessian matrix of second derivatives of travel- time. For the derivatives with respect to the intersection of the ray with the ith layer (the segment from (x_i, y_i, z_i) to $(x_{i+1}, y_{i+1}, z_{i+1})$), only the seven elements within the dashed lines need to be calculated.

	x_{i-1}	y_{i-1}	x_i	y_i	x_{i+1}	y_{i+1}
x_{i-1}	$\frac{\partial^2 T}{\partial x_{i-1}\partial x_{i-1}}$	$\frac{\partial^2 T}{\partial y_{i-1}\partial x_{i-1}}$	$\frac{\partial^2 T}{\partial x_i \partial x_{i-1}}$	$\frac{\partial^2 T}{\partial y_i \partial x_{i-1}}$		
y_{i-1}		$\frac{\partial^2 T}{\partial y_{i-1}\partial y_{i-1}}$	$\frac{\partial^2 T}{\partial x_i \partial y_{i-1}}$	$\frac{\partial^2 T}{\partial y_i \partial y_{i-1}}$		
x_i			$\frac{\partial^2 T}{\partial x_i \partial x_i}$	$\frac{\partial^2 T}{\partial y_i \partial x_i}$	$\frac{\partial^2 T}{\partial x_{i+1}\partial x_i}$	$\frac{\partial^2 T}{\partial y_{i+1}\partial x_i}$
y_i				$\frac{\partial^2 T}{\partial y_i \partial y_i}$	$\frac{\partial^2 T}{\partial x_{i+1}\partial y_i}$	$\frac{\partial^2 T}{\partial y_{i+1}\partial y_i}$
x_{i+1}					$\frac{\partial^2 T}{\partial x_{i+1}\partial x_{i+1}}$	$\frac{\partial^2 T}{\partial y_{i+1}\partial x_{i+1}}$
y_{i+1}						$\frac{\partial^2 T}{\partial y_{i+1}\partial y_{i+1}}$

$$\frac{\partial^2 T}{\partial X_i \partial X_j}$$

$$\Delta X_j = -\frac{\partial T}{\partial X_i}, \qquad \text{(A-10)}$$

spacewhere ΔX is the vector of updates to the x and y intersections, and we must calculate both the first and second partial deriva- tives of traveltime with respect to the elements of X . Due to the form of equation (A-7), only contributions from adjacent layers remain in the partial derivatives. Any second derivative

$$F(x,y) = +C_0 + C_1 x + C_2 y + C_3 xy + C_4(2x^2 - 1) + C_5(2y^2 - 1) + C_6(2x^2 - 1)y + C_7(2y^2 - 1)x + C_8(4x^3 - 3x) + C_9(4y^3 - 3y). \qquad (1)$$

$$t = \int_A^B S(x,y)\, dl, \qquad (2)$$

APPENDIX A

CALCULATION OF TRAVELTIME AND LINEAR SYSTEM OF EQUATIONS USED FOR RAY TR

Parametric traveltime calculation

The line integrals for traveltime in our model are calculated in parametric form. The equations for the 2-D third-order Chebyshev polynomials and the traveltime within a single layer are repeated here from equations (1) and (2):

$$\begin{aligned} S(x,y) = {} & C_0 + C_1x + C_2y + C_3xy + C_4(2x^2-1) \\ & + C_5(2y^2-1) + C_6(2x^2-1)y + C_7(2y^2-1)x \\ & + C_8(4x^3-3x) + C_9(4y^3-3y), \end{aligned} \tag{A-1}$$

$$t = \int_A^B S(x,y)dl. \tag{A-2}$$

Here, C_0 through C_9 are the polynomial coefficients, and A and B have the coordinates (x_1, y_1, z_1) and (x_2, y_2, z_2), according to Figure 4. First, we express x, y, and z in parametric form:

$$\begin{aligned} x &= x_1 + \sigma\delta x \quad \delta x = (x_2 - x_1), \\ y &= y_1 + \sigma\delta y \quad \delta y = (y_2 - y_1), \\ z &= z_1 + \sigma\delta z \quad \delta z = (z_2 - z_1). \end{aligned} \tag{A-3}$$

The parameter σ ranges from 0 to 1, and by substitution we can replace equation (A-1) with one that involves only σ and the constants $(x_1, y_1, \delta x, \delta y)$:

$$\begin{aligned} S(\sigma) = {} & C_0 + C_1[\sigma\delta x + x_1] + C_2[\sigma\delta y + y_1] \\ & + C_3[\sigma^2\delta x\delta y + x_1\sigma\delta y + y_1\sigma\delta x + x_1y_1] \\ & + C_4[2\sigma^2\delta x^2 + 4x_1\sigma\delta x + 2x_1^2 - 1] \\ & + C_5[2\sigma^2\delta y^2 + 4y_1\sigma\delta y + 2y_1^2 - 1] \\ & + C_6[2\sigma^3\delta x^2\delta y + 4x_1\sigma^2\delta x\delta y + 2x_1^2\sigma\delta y \\ & + 2y_1\sigma^2\delta x^2 + 4x_1y_1\sigma\delta x + \sigma\delta y + 2x_1^2y_1 + y_1] \\ & + C_7[2\sigma^3\delta y^2\delta x + 4y_1\sigma^2\delta y\delta x + 2y_1^2\sigma\delta x \\ & + 2x_1\sigma^2\delta y^2 + 4y_1x_1\sigma\delta y + \sigma\delta x + 2y_1^2x_1 + x_1] \\ & + C_8[4\sigma^3\delta x^3 + 12x_1\sigma^2\delta x^2 + 12x_1^2\sigma\delta x + 3\sigma\delta x \\ & + 3x_1 + 4x_1^3] + C_9[4\sigma^3\delta y^3 + 12y_1\sigma^2\delta y^2 \\ & + 12y_1^2\sigma\delta y + 3\sigma\delta y + 3y_1 + 4y_1^3]. \end{aligned} \tag{A-4}$$

The variable ℓ is the length along the straight-line segment of the ray, and we find the required change of variable to the parameter σ for the integral:

$$\begin{aligned} \ell &= [(x-x_1)^2 + (y-y_1)^2 \\ &= [\sigma^2(\delta x^2 + \delta y^2 + \delta z^2)]^{\frac{1}{2}} \\ \frac{dl}{d\sigma} &= (\delta x^2 + \delta y^2 + \delta z^2)^{\frac{1}{2}}. \end{aligned}$$

The traveltime integral then becomes

$$t = (\delta x^2 + \delta y^2 + \delta z^2)^{\frac{1}{2}} \int_0^1 S($$

Finally, after integration over σ, the trav layer becomes

$$\begin{aligned} t = {} & [(x_2 - x_1)^2 + (y_2 - y_1)^2 + (z_2 \\ & + C_1\frac{1}{2}(x_1 + x_2) + C_2\frac{1}{2}(y_1 + y_2 \\ & + C_3\left[\frac{1}{3}(x_1y_1 + x_2y_2) + \frac{1}{6}(x_1y_2\right. \\ & + C_4\left[\frac{2}{3}(x_1^2 + x_1x_2 + x_2^2) - 1\right] \\ & + C_5\left[\frac{2}{3}(y_1^2 + y_1y_2 + y_2^2) - 1\right] \\ & + C_6\left[\frac{1}{2}x_1^2y_1 + \frac{1}{6}x_1^2y_2 + \frac{1}{3}(x_1x_2\right. \\ & + \frac{1}{6}x_2^2y_1 + \frac{1}{2}x_2^2y_2 - \frac{1}{2}(y_1 + y_2 \\ & + C_7\left[\frac{1}{2}y_1^2x_1 + \frac{1}{6}y_1^2x_2 + \frac{1}{3}(y_1y_2\right. \\ & + \frac{1}{6}y_2^2x_1 + \frac{1}{2}y_2^2x_2 - \frac{1}{2}(x_1 + x_2 \\ & + C_8\left[x_1^3 + x_2^3 + x_1^2x_2 + x_1x_2^2\right. \\ & + C_9\left[y_1^3 + y_2^3 + y_1^2y_2 + y_1y_2^2\right. \end{aligned}$$

We can observe from the form of this derivatives of traveltime can be calcu In particular the derivatives with respe

coefficients, used for the velocity inversion, are very simple to determine.

For a ray that passes through n layers, the total traveltime is then

$$T = \sum_{i=1}^{n} t_i. \tag{A-8}$$

The linear system of equations used for ray tracing

As described earlier, ray tracing is performed via the bending method. We can take advantage of the structural stratification of the model, and treat z as a function of x and y on each of the surfaces that a ray intersects. We then only need to solve for updates to x and y at each surface. For each ray, we first organize the x and y intersections for the n layers the ray passes through into a vector of length $2n$:

$$X = (x_1, y_1, x_2, y_2, \ldots, x_n, y_n). \tag{A-9}$$

We solve the minimization problem by using Newton's method to find the critical points of the objective function. In each iteration, we have the following linear system:

$$\frac{\partial^2 T}{\partial X_i \partial X_j} \Delta X_j = -\frac{\partial T}{\partial X_i}, \tag{A-10}$$

where ΔX is the vector of updates to the x and y intersections, and we must calculate both the first and second partial derivatives of traveltime with respect to the elements of X. Due to the form of equation (A-7), only contributions from adjacent layers remain in the partial derivatives. Any second derivative with respect to elements of X more than
zero. The Hessian matrix of second deriv
is therefore symmetric and band-diagona
ments in only three super-diagonals. Table
of the Hessian. For the derivatives with
section of the ray with the ith layer, only
within the dashed lines in Table A-1 need

**Table A-1. Hessian matrix of second d
time. For the derivatives with respect to
the ray with the ith layer (the segmen
$(x_{i+1}, y_{i+1}, z_{i+1})$), only the seven element
lines need to be calculated.**

	x_{i-1}	y_{i-1}	x_i	y_i
x_{i-1}	$\frac{\partial^2 T}{\partial x_{i-1}\partial x_{i-1}}$	$\frac{\partial^2 T}{\partial y_{i-1}\partial x_{i-1}}$	$\frac{\partial^2 T}{\partial x_i \partial x_{i-1}}$	$\frac{\partial^2 T}{\partial y_i \partial x_{i-1}}$
y_{i-1}		$\frac{\partial^2 T}{\partial y_{i-1}\partial y_{i-1}}$	$\frac{\partial^2 T}{\partial x_i \partial y_{i-1}}$	$\frac{\partial^2 T}{\partial y_i \partial y_{i-1}}$
x_i			$\frac{\partial^2 T}{\partial x_i \partial x_i}$	$\frac{\partial^2 T}{\partial y_i \partial x_i}$
y_i				$\frac{\partial^2 T}{\partial y_i \partial y_i}$
x_{i+1}				
y_{i+1}				